Computers in Biology and Medicine 210 (2026) 111715

Contents lists available at ScienceDirect

Computers in Biology and Medicine

journal homepage: www.elsevier.com/locate/compbiomed

A personalized mechanobiology-driven multiscale model of atherosclerosis

Ricardo Caballero[a,*], Miguel Ángel Martínez[a,b], Jolanda J. Wentzel[c], Ali C. Akyildiz[c,d], Estefanía Peña[a,b]

[a] Aragón Institute of Engineering Research (I3A), University of Zaragoza, Zaragoza, Spain
[b] Biomedical Research Networking Center in Bioengineering, Biomaterials and Nanomedicine (CIBER-BBN), Zaragoza, Spain
[c] Department of Cardiology, Biomedical Engineering, Cardiovascular Institute, Thorax Center, Erasmus MC, University Medical Center Rotterdam, Rotterdam, the Netherlands
[d] Department of Biomechanical Engineering, Delft University of Technology, Delft, the Netherlands

HIGHLIGHTS

- A hybrid CFD-transport-ABM framework was validated in porcine coronaries.
- The model linked baseline hemodynamics to later plaque progression patterns.
- Predicted outputs included stenosis progression and arterial wall thickening.
- Low-WSS regions were associated with lipid accumulation and eccentric growth.
- The framework reproduced the locations of lipid-rich and necrotic regions.

ARTICLE INFO

Keywords:
Atherosclerosis
Computational fluid dynamics
Mass transport
Agent-based model
Multiscale modeling
Porcine coronary arteries

ABSTRACT

Atherosclerosis is a chronic inflammatory and metabolic disease primarily driven by systemic lipid imbalances, with plaque localization and progression further modulated by local hemodynamic and cellular factors within the arterial wall. Here we present a validation study of a hybrid multiscale model that couples computational fluid dynamics (CFD), mass-transport-driven low-density lipoprotein (LDL) maps, and an agent-based model (ABM) of cell behavior to predict coronary plaque initiation and progression. Validation employed adult minipigs carrying a low-density lipoprotein receptor (LDLR) mutation—an established preclinical analogue of human hypercholesterolemia—using longitudinal in vivo imaging data collected within the BIOCCORA study, with 1-year follow-up capturing plaque initiation and evolution. By linking wall shear stress (WSS)-dependent LDL filtration with cytokine-guided smooth muscle cell (SMC) activity, the model mechanistically reconstructs the plaque microenvironment rather than fitting outcomes post hoc. Tested on four imaging-derived porcine coronary arteries tracked over time, the model anticipates where and how fast plaques grow and how lipid pools evolve across cross-sections, showing strong concordance with experiments. These results position hybrid multiscale in silico models as promising predictors for disease progression and could aid in future treatment decision-making.

1. Introduction

Atherosclerosis is widely recognized as the leading cause of cardiovascular diseases (CVDs), accounting for approximately 32% of all deaths globally [1–3]. Its progression is modulated by genetic predisposition and modifiable risk factors such as dyslipidemia, hypertension, diabetes, smoking, and obesity [4–8]. These factors critically affect endothelial cell (EC) function, increasing the propensity for endothelial-to-mesenchymal transition and barrier disruption [9–12].

Atherosclerosis is considered a progressive inflammatory disease characterized by the accumulation of lipids, immune cells, and extracellular matrix (ECM) within the arterial wall. Triggered by endothelial dysfunction and increased vascular permeability, an innate immune response drives arterial remodeling and plaque development [13]. The resulting structural alterations typically involve an early phase of compensatory outward remodeling, known as Glagov remodeling, which preserves luminal area despite plaque growth, followed by a later stage

* Corresponding author.
Email address: rcaballero@unizar.es (R. Caballero).

https://doi.org/10.1016/j.compbiomed.2026.111715
Received 14 January 2026; Received in revised form 15 April 2026; Accepted 24 April 2026
Available online 5 May 2026

in which inward remodeling leads to progressive lumen narrowing and clinical consequences [14].

From a biomechanical perspective, disturbed blood flow generates regions of low wall shear stress (WSS), which are consistently associated with atheroprone patches. As WSS decreases, endothelial permeability increases, facilitating the expression of adhesion molecules and the release of pro-inflammatory cytokines, thereby amplifying leukocyte recruitment and vascular inflammation [15,16].

The earliest stages of plaque formation begin with the subendothelial retention of low-density lipoproteins (LDL) and their subsequent oxidation into oxLDL. This process activates endothelial cells and stimulates the expression of adhesion molecules [17], which recruit circulating monocytes into the intima where they differentiate into macrophages (MCs) [18]. MCs internalize oxLDL and secrete pro-inflammatory cytokines, driving local inflammation [19]. Once their lipid uptake capacity is overwhelmed, MCs transform into foam cells (FCs). The accumulation and secondary necrosis of these FCs ultimately constitute the plaque's lipid-rich necrotic core [20,21]. Concurrently, vascular smooth muscle cells (vSMCs) in the media layer become activated. Normally, these cells maintain vascular tone in a quiescent, contractile phenotype (cSMCs). However, during plaque formation, they switch to a synthetic phenotype (sSMCs), acquiring the ability to migrate, proliferate, and produce extracellular matrix (ECM). Together, continuous FC accumulation and the sSMC-mediated immune response drive plaque expansion, resulting in arterial wall thickening and luminal narrowing [22–25].

Computational modeling has emerged as a powerful tool to investigate the mechanobiological processes underlying atherosclerosis. Foundational approaches rely on the Navier-Stokes and continuity equations to describe luminal blood flow and its coupling with mass transport theories [26]. Building on this, personalized computational fluid dynamics (CFD) simulations have been extensively used to clarify the interrelation among altered hemodynamics, LDL accumulation, and hypoxia in patient-specific geometries, explaining the localization of plaques in predilection sites [27–30]. Beyond traditional mass transport, recent clinical and computational efforts have focused on identifying robust biomechanical predictors of plaque progression. While time-averaged WSS (TAWSS) is widely studied, novel metrics such as the topological shear variation index (TSVI) better capture the variability of contraction and expansion actions on the endothelium. When combined with intravascular imaging (e.g., NIRS, OCT, IVUS), the synergistic effect of high TSVI, low TAWSS, and a lipid-rich phenotype has been shown to strongly predict enhanced plaque progression [31]. To further understand lipid infiltration, advanced mechanobiological models have coupled luminal hemodynamics with arterial wall mechanics. These frameworks typically employ Darcy's law and the Kedem-Katchalsky equations for endothelial filtration, alongside convection-diffusion-reaction equations to describe substance transport within the wall [32–34]. Such models, driven by extensive sensitivity analyses [34], have demonstrated how biomechanical factors like hypertension—modeled through hyperelastic constitutive laws (e.g., Yeoh's model)—increase plaque volume via wall compaction [32]. Furthermore, incorporating dynamic geometric and hemodynamic updating has allowed these models to reproduce complex disease progression features, such as the double-stenosis phenomenon [33]. While these continuous approaches—typically based on partial differential equations (PDEs)—have profoundly clarified the relationship between disturbed hemodynamics, mechanical stress, and lipid infiltration, they represent biological entities as continuous concentrations. Consequently, many do not explicitly resolve the discrete, cellular-level biological responses—including inflammation, cellular migration, and tissue remodeling—that ultimately drive plaque growth [35].

To overcome this limitation, Agent-Based Models (ABMs) have been introduced as a bottom-up modeling methodology, where simple rules defined at the individual level allow for the understanding of complex, higher-level phenomena. In an ABM framework, the system is composed of autonomous and heterogeneous agents—such as distinct immune and vascular cells—that make decisions and take actions based on their internal state and local microenvironment. Through continuous interactions among themselves and with their environment, these agents generate emergent behavior: the global macroscopic dynamics of the plaque are not pre-programmed, but rather arise naturally from local cellular interactions. In the context of atherosclerosis, this approach is highly advantageous, as it allows the assignment of specific, rule-based biological behaviors (e.g., macrophage phagocytosis, smooth muscle cell phenotype switching, and apoptosis) to individual cells. As highlighted in recent comprehensive reviews [36], multiscale frameworks based on ABMs offer a biologically realistic representation by naturally capturing morphological heterogeneity, localized cell-cell and cell-matrix interactions, and the stochastic nature of biological processes.

Importantly, hybrid multiscale coupling strategies combining continuum hemodynamics and transport with ABM-based descriptions of tissue adaptation have also been conceptualized in related vascular remodeling contexts (e.g., restenosis and vascular adaptation), providing further support for the rationale of hybrid modeling [37–39]. Ultimately, this bottom-up strategy enables the simulation of emergent tissue-level phenomena, such as the formation of the necrotic core, which are fundamentally difficult to capture with conventional PDEs [40].

Despite substantial progress in computational modeling of atherosclerosis, coupling hemodynamics and mass transport to ABM-driven plaque development remains scarce. Alongside our previously published foundational framework [41], very recent and valuable efforts have begun to apply these hybrid methodologies to evaluate plaque progression in human coronary arteries [42]. Notably, [42] represents an important step forward by providing validation against human coronary imaging data, demonstrating the clinical applicability of such hybrid frameworks. Nevertheless, a complementary validation challenge remains: testing these coupled models against controlled, time-resolved in vivo data of early plaque initiation, a phase that is inherently difficult to capture longitudinally in human cohorts. This validation challenge arises from the multifactorial nature of atherosclerosis and the limited availability of longitudinal, high-resolution biological data [20]. In humans, ethical and practical constraints preclude prospective studies focused on the earliest stages of lesion development, and most clinical datasets capture plaques only after they are already established. In this context, porcine models are particularly valuable because their coronary anatomy and pathophysiology resemble those of humans, while enabling controlled serial imaging and histological assessment of plaque development over time [43]. Although interspecies differences remain and are beyond the scope of this work, such models provide a uniquely suitable platform for validation of mechanobiology-based multiscale frameworks.

Starting from our previously published framework [41], we extended the model and performed its calibration and longitudinal validation against porcine experimental data in a preclinical coronary setting. First, we replaced the former steady-state flow assumption with fully transient CFD simulations of pulsatile coronary hemodynamics, enabling a more physiological representation of flow-driven stimuli. Second, the model was applied to imaging-derived porcine coronary geometries obtained from a longitudinal intravascular study providing serial medical imaging, reconstructable coronary geometries, and associated hemodynamic information over long-term follow-up—a combination of data that is seldom available for validation of computational models of atherosclerosis. These serial in vivo measurements enable direct validation of the coupled hemodynamic–transport–agent-based framework against plaque progression over time, rather than static end-point observations. Together, these developments allow a mechanobiologically consistent reproduction of plaque initiation and progression and, to the best of our knowledge, establish one of the first hybrid frameworks that integrates hemodynamics, LDL transport, and agent-based tissue remodeling within a single multiscale model for porcine coronary atherosclerosis.

Paper organization. The remainder of this manuscript is structured as follows. The Methods section describes the experimental dataset and the hybrid multiscale modeling framework, detailing the 3D hemodynamics module, the 2D mass-transport model, and the cellular dynamics components, as well as the coupling and validation strategies. The Results section presents the parameter calibration and the qualitative and quantitative validation results, including the assessment of spatial patterns of wall thickening and lipid accumulation across different hemodynamic scenarios. The Discussion section analyzes the clinical relevance of the framework, its current limitations, and future directions for model enhancement. Finally, the Conclusions section summarizes the main contributions and findings of this study.

2. Methods

Originally calibrated for humans [41], the framework was adapted for porcine validation on the BIOCCORA dataset [44], which offers in vivo coronary flow waveforms across the cardiac cycle together with one-year longitudinal imaging. This enabled qualitative and quantitative evaluations. Time scales, parameters, and coupling cadence were recalibrated to match the dataset's acquisition schedule and temporal resolution.

2.1. Experimental dataset

The BIOCCORA project generated a longitudinal in vivo porcine imaging dataset capturing key hemodynamic and pathological features of coronary atherosclerosis. The experimental design, animal preparation, and the specific dataset utilized in this work are comprehensively described in key previous publications [43,44]. Briefly, a cohort of adult familial hypercholesterolemic minipigs carrying a homozygous LDL receptor (LDLR) mutation was maintained on a high-fat diet for over one year to induce plaque formation. Intravascular imaging was performed at baseline (T1, three months after diet initiation), at an intermediate follow-up (T2, nine months), and at the endpoint (T3, twelve months), enabling longitudinal tracking of lesion development in vivo (Fig. 1).

At each imaging session, the animals were anesthetized and instrumented for coronary catheterization. Serial pullbacks combining intravascular ultrasound (IVUS) and optical coherence tomography (OCT) were acquired along the major coronary arteries, complemented by Doppler velocity and pressure measurements (ComboWire) at multiple axial locations. IVUS provided full-wall cross-sectional information for lumen and external elastic lamina (EEL) segmentation, while OCT offered micrometric resolution of the intimal surface, enabling identification of lipid-rich regions as signal-poor areas with diffuse borders and characteristic attenuation. These were annotated as binary lipid indicators for each frame.

For this validation study, we selected four coronary arteries from two pigs enrolled in the BIOCCORA cohort: two left anterior descending (LAD) and two right coronary arteries (RCA). The original study comprised ten animals, five of which developed mild coronary disease and five exhibited advanced coronary disease. From this latter subgroup, we selected two pigs that showed the highest burden of lipid-rich plaque, as identified by OCT, in order to focus the validation on arteries with pronounced pathological remodeling and clear longitudinal progression between baseline and follow-up. Although the original study included a twelve-month time point, the present analysis focused on the first nine months (T1-T2) to ensure consistent comparison, as one animal did not reach the final session. For this study, each artery was discretized into 50 cross-sections. This sampling was chosen to approximately match the longitudinal resolution of the intravascular dataset (about one frame every ~3 mm), to provide a sufficiently large number of spatial validation points for statistical analysis, and to support accurate 3D reconstruction. CFD-derived hemodynamic and transport fields were mapped onto these sections for subsequent 2D ABM simulations. For qualitative illustration, however, only $n = 3$ representative cross-sections per artery are highlighted in the Results section. These cross-sections were chosen to illustrate distinct phenotypic scenarios: one with substantial plaque growth, one with moderate progression, and one with minimal or no change. Fig. 2 summarizes the imaging and computational workflow, from coronary segmentation and Doppler-informed CFD analyses to the extraction of morphometric metrics, namely stenosis ratio (SR) and wall thickening (ΔWT) between T1 and T2.

2.2. Hybrid multiscale model overview

Our hybrid multiscale computational framework couples processes spanning temporal (seconds to months) and spatial (molecules to organ) scales by integrating three coupled components (Fig. 3): (*i*) a CFD module that resolves 3D coronary hemodynamics at the organ-tissue level and yields TAWSS over the cardiac cycle (seconds); (*ii*) a 2D mass-transport module that models convection, diffusion, and reaction underlying endothelial filtration of LDL and the subsequent intramural accumulation and oxidation (molecular scale, seconds to days); and (*iii*) a 2D ABM that captures cell-level inflammatory and immune dynamics—MCs recruitment, vSMCs migration and proliferation, FCs formation, and ECM turnover—driving tissue-level remodeling (cellular to tissue scales, days to months). Information flows through well-defined coupling variables (Fig. 4): TAWSS maps from CFD modulate endothelial permeability and hence LDL influx in the transport module; the resulting spatiotemporal fields of oxLDL serve as input to the ABM; and the ABM outputs (e.g., local wall thickening and evolving plaque morphology) feed back to update lumen geometry and flow boundary conditions in the continuum models, thereby closing the multiscale feedback loop

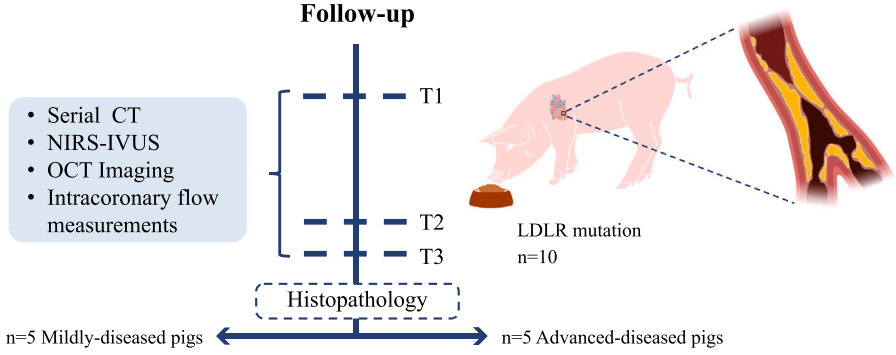

Fig. 1. Overview of the BIOCCORA study design. LDLR mutated pigs were maintained on a high-fat diet for one year to induce coronary atherosclerosis. Intravascular imaging was performed at three time points: baseline (T1, 3 months after diet initiation), intermediate follow-up (T2, 9 months), and endpoint (T3, 12 months). Invasive imaging techniques employed included CT, NIRS-IVUS, OCT, and intracoronary flow measurements, enabling longitudinal tracking of plaque development. After sacrifice, histopathological analysis was performed for validation.

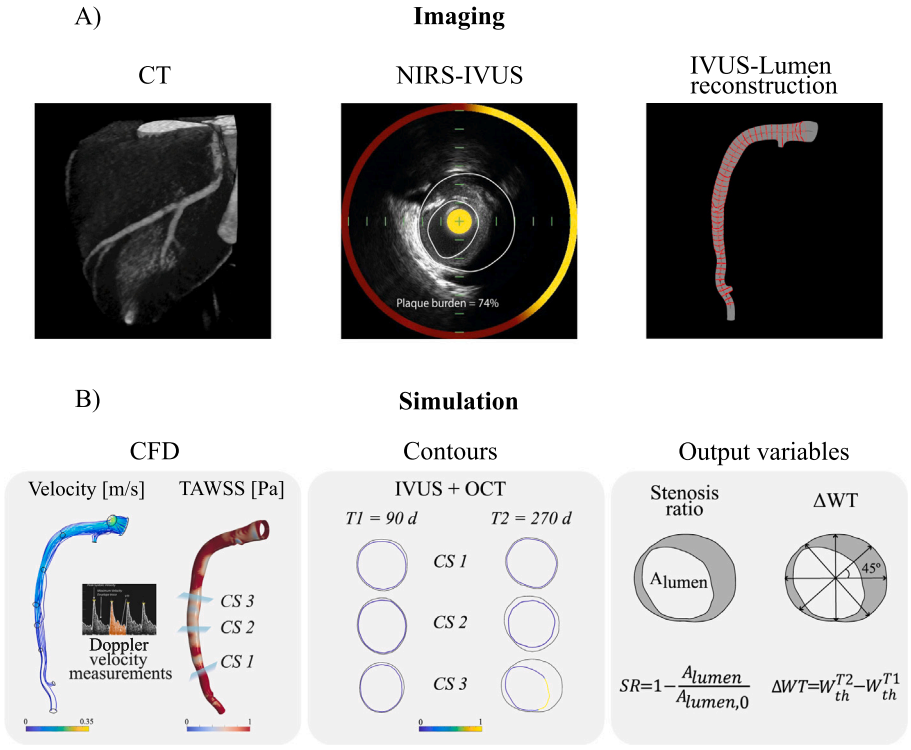

Fig. 2. Overview of the experimental imaging and simulation pipeline used to generate the validation dataset. (A) imaging workflow: Computed Tomography coronary Angiography (CTCA) was used to identify the target segment and obtain the centerline, followed by NIRS-IVUS imaging to quantify plaque burden and tissue composition. IVUS pullbacks were reconstructed into 3D lumen and vessel-wall geometries after co-registration with CTCA. (B) simulation workflow: baseline (T1) lumen and wall contours were used to perform transient CFD analyses to obtain TAWSS maps. Intravascular Doppler measurements were processed to derive subject-specific flow information and were used to prescribe the inlet inflow waveform and, when applicable, to constrain outlet flow splits in the CFD boundary conditions. Corresponding IVUS-OCT contours at baseline and follow-up (T2) enabled quantification of morphometric changes such as SR and ΔWT.

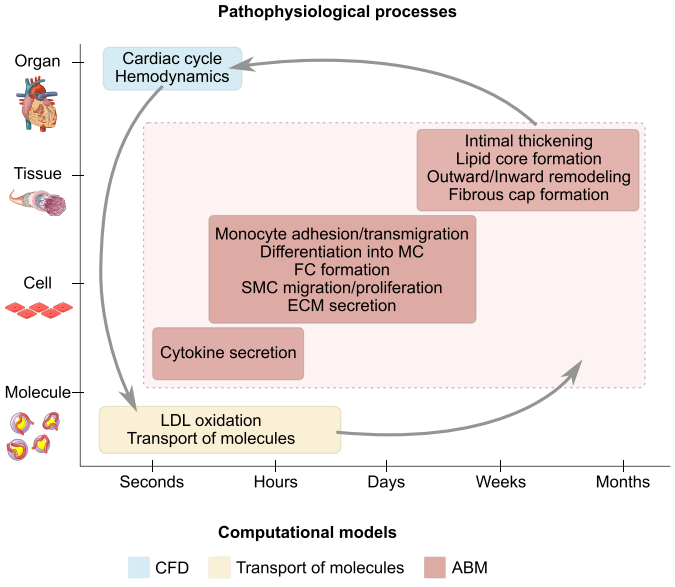

Fig. 3. Schematic representation of the multiscale framework of atherosclerosis. The figure integrates two dimensions of analysis: the spatial scale (molecular, cellular, tissue, and organ levels) and the temporal scale (from seconds to months). The main pathophysiological processes are distributed across these scales, while the colored boxes indicate the computational models used to reproduce them: CFD (blue), transport phenomena (green), and ABM (red). Together, these approaches capture the multiscale nature of plaque development and vascular remodeling. Within this framework, hemodynamics are placed at the organ level because they depend on systemic cardiac function, whereas the vessel wall itself is represented at the tissue level, where structural remodeling occurs.

and linking molecular and cellular mechanisms to macroscopic vessel remodeling.

2.3. 3D hemodynamics (CFD)

The objective of the 3D hemodynamic model is to obtain reliable distributions of TAWSS that can serve as input for the subsequent 2D mass-transport simulations. Time-dependent CFD simulations on the baseline (T1) 3D coronary geometries were performed within the BIOCCORA study using ANSYS Fluent (v.17.1, ANSYS Inc., Canonsburg, PA, USA), following the workflow and numerical settings previously described [45]. In the present work, these CFD results were not recomputed; instead, we post-processed the baseline BIOCCORA CFD outputs to extract cross-sectional 2D TAWSS maps used as inputs for the mass-transport and ABM modules.

Governing equations and material properties. Blood was modeled as an incompressible, homogeneous Newtonian fluid with density $\rho = 1050\ \mathrm{kg/m^3}$ and dynamic viscosity $\mu = 0.0035\ \mathrm{Pa \cdot s}$. Vessel walls were assumed to be rigid with a no-slip boundary condition. The unsteady Navier–Stokes equations were solved as

$$\rho\left(\frac{\partial \mathbf{u}}{\partial t} + (\mathbf{u}\cdot\nabla)\mathbf{u}\right) = -\nabla p + \mu\nabla^2\mathbf{u}, \qquad \nabla\cdot\mathbf{u} = 0, \tag{1}$$

where $\mathbf{u}$ is the velocity field and p is the pressure.

Boundary conditions. Pig-specific, time-varying inlet and outlet boundary conditions were derived from in vivo ComboWire Doppler velocity measurements, as previously described [44,45]. The most proximal high-quality Doppler waveform was applied at the inlet as a time-dependent flat velocity profile. For each side branch, the flow split

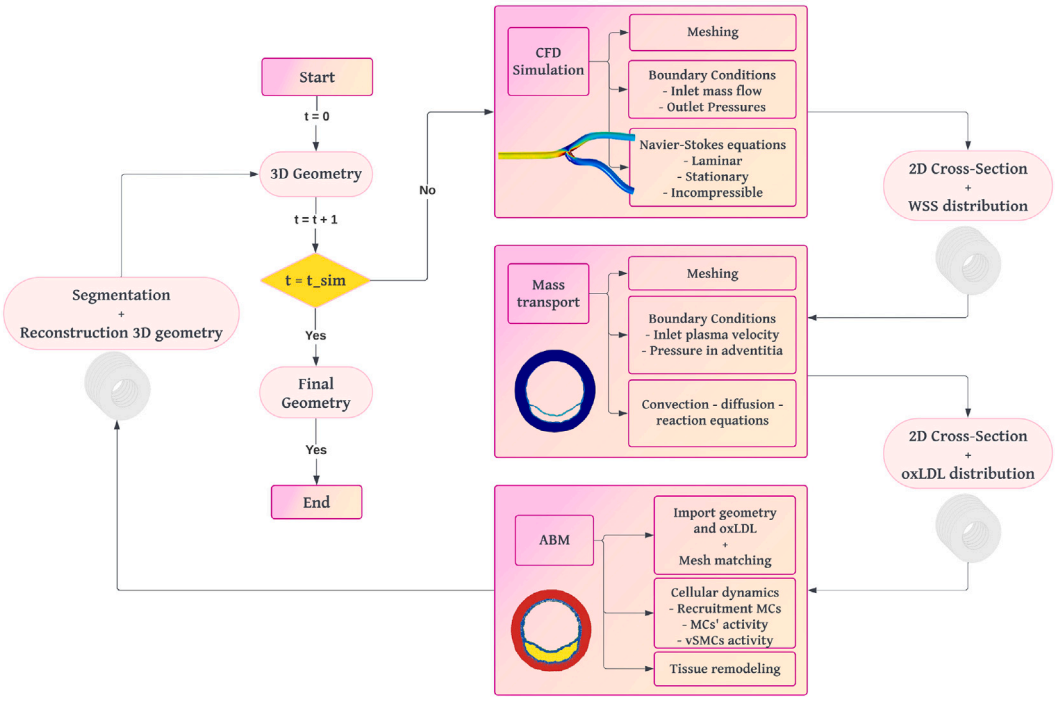

Fig. 4. Workflow diagram of the fully coupled multiscale framework for plaque growth reproduction. The process begins with a 3D geometry of a healthy artery. CFD simulations calculate TAWSS. Mass transport simulations determine oxLDL distribution. An ABM simulates cellular dynamics to compute plaque growth and vessel remodeling. The iterative process updates the 3D geometry until the final simulation time is reached. Figure reproduced from our previous work [41].

was calculated from the difference between upstream and downstream Doppler-based flow measurements and imposed as the outflow condition.

Mesh generation. Computational domains were discretized using unstructured, curvature-based tetrahedral meshes including five boundary layers adjacent to the lumen to adequately resolve near-wall gradients. Mesh resolution was selected based on a mesh-sensitivity analysis targeting less than 1% variation in TAWSS metrics, yielding meshes of approximately 6×10^6 elements on average and a characteristic element size of ~ 0.05 mm [45].

Numerical setup. The BIOCCORA transient simulations were run over multiple cardiac cycles until a periodic state was reached [45]. Spatial discretization employed second-order accuracy for both momentum and pressure, using the COUPLED pressure–velocity coupling scheme [45]. Time integration used a backward Euler implicit scheme with a fixed time increment, with each cardiac cycle discretized using 100 time steps. In the present work, the cardiac periods were $T = 1.03$ s for Pig #1 and $T = 0.67$ s for Pig #2 (i.e., $\Delta t = 0.0103$ s and $\Delta t = 0.0067$ s, respectively). Convergence at each time step was achieved when continuity and momentum residuals fell below 10^{-5} [45].

Hemodynamic post-processing. To avoid residual start/end effects in waveform-driven transient simulations and to ensure that time-averaged indices were computed under periodic conditions, we extracted data over the final 1.5 cardiac cycles of each simulation. Hemodynamic metrics were then computed over the last full cardiac cycle within this window (i.e., after discarding the preceding half-cycle).

Hemodynamic metrics. The hemodynamic index analyzed was the TAWSS, computed on the luminal surface as

$$\mathrm{TAWSS} = \frac{1}{T}\int_0^T \left|\boldsymbol{\tau}_w(t)\right| \, dt \tag{2}$$

where $\boldsymbol{\tau}_w(t)$ is the instantaneous WSS vector and T is the duration of one cardiac cycle. The integral was evaluated pointwise over the vessel wall surface using the final periodic cardiac cycle extracted as described above.

2.4. Mass transport model

A 2D mass transport model was implemented on cross-sectional arterial domains extracted from the 3D geometries. The computational domain represented the arterial cross-section and comprised the lumen together with the wall layers: endothelium, intima, IEL, media, and EEL. This choice was motivated by the scope of the present transport and ABM modules, which focus on intima–media mechanisms of plaque development. Atherosclerotic lesions originate in the intima, where lipid accumulation, endothelial dysfunction, and inflammatory cell recruitment primarily occur, with subsequent involvement of the media during plaque growth and remodeling [46]. Although the adventitia may contribute to vascular inflammation, particularly through vasa vasorum–associated pathways, these outside-in mechanisms were beyond the scope of the present framework and were therefore not explicitly modeled. Therefore, omitting the adventitia allowed us to restrict the model to the layers directly involved in luminal-driven transport and intima–media immune responses while reducing computational complexity. Although the endothelium is often considered part of the intima in anatomical classifications, it was explicitly modeled here as a distinct functional layer. Together with the IEL, it was treated as a porous barrier regulating the transwall transport of substances through its pores, with permeability and selectivity modulated by local conditions.

Plasma and LDL transport across the arterial wall was modeled with a porous-media formulation, originally proposed by [28], that couples plasma filtration with LDL convection-diffusion-reaction. The governing equations are discussed below and summarized in Tables 1 and 2.

The interstitial plasma velocity $\mathbf{u_p}$ was obtained from Darcy's law (Eq. 3), relating it to the pressure gradient (∇P), local hydraulic permeability (k_ℓ), and plasma viscosity (μ_p). At the endothelium, the

Table 1
Plasma filtration equations and relationships.

Definition	Equation	
Plasma filtration velocity in the wall (layer ℓ)	$\mathbf{u}_p = -\frac{k_\ell}{\mu_p}\nabla P, \quad \ell \in \{\text{int}, \text{med}\}$	(3)
Filtration flux (Starling's law)	$J_v = L_p \Delta P$	(4)
Three-pore decomposition of plasma flux	$J_v = J_{v,nj} + J_{v,lj} + \cancel{J_{v,vp}}$	(5)
Flux through normal junctions	$J_{v,nj} = L_{p,nj} \Delta P_{\text{end}}$	(6)
Hydraulic conductivity due to normal junctions	$L_{p,nj} = \Phi_{nj} L_{p,snj}$	(7)
Flux through leaky junctions	$J_{v,lj} = L_{p,lj} \Delta P_{\text{end}}$	(8)
Hydraulic conductivity due to leaky junctions	$L_{p,lj} = \Phi_{lj} L_{p,slj}$	(9)
Area fraction of normal junctions	$\Phi_{nj} = 1 - \Phi_{lj}$	(10)
Area fraction of leaky junctions	$\Phi_{lj} = \frac{A_{lj}}{A_{\text{T}}} = \frac{4\,w_l}{R_{\text{cell}}}\Phi_{LC}$	(11)
Endothelial area fraction occupied by leaky cells	$\Phi_{LC} = \frac{LC \cdot \pi R_{\text{cell}}^2}{A_{\text{unit}}}$	(12)
Leaky cells as a function of mitotic cells	$LC = 0.307 + 0.805\,MiC$	(13)
Mitotic cells per unit area as a function of shape index	$MiC = 0.003797\, e^{14.75\,SI}$	(14)
Shape Index as a function of TAWSS	$SI = 0.380\, e^{-0.790\,\text{TAWSS}} + 0.225\, e^{-0.043\,\text{TAWSS}}$	(15)

transendothelial plasma flux J_v followed a simplified Starling's law driven by the transmural pressure drop ΔP_{end} and the hydraulic conductivity (L_p), neglecting osmotic terms (Eq. 4).

Endothelial permeability was represented through the three-pore theory [47], which decomposes the overall volumetric plasma flux into normal junctions ($J_{v,nj}$), leaky junctions ($J_{v,lj}$), and vesicular pathways ($J_{v,vp}$). The vesicular contribution was considered negligible, so that plasma flow occurs primarily through normal and leaky junctions [29] (Eq. 5). Regions exposed to low TAWSS are known to promote a pro-atherogenic endothelial phenotype, including impaired mechanotransduction and altered cell morphology, which has been associated with increased endothelial permeability [12]. Specifically, endothelial dysfunction was incorporated through an empirical relation between TAWSS and the endothelial shape index (SI) (Eq. 15). The endothelial SI is a dimensionless descriptor of cell morphology, commonly defined from projected area A and perimeter P (e.g., $SI = 4\pi A/P^2$), where higher values indicate more rounded shapes and lower values indicate more elongated shapes [48]. This index determines the density of mitotic cells (Eq. 14) and leaky cells (Eq. 13), thereby modulating the area fraction of leaky junctions (Eq. 11) and ultimately the hydraulic conductivity of the endothelium (Eq. 9).

The transport of LDL within the intima was governed by a convection-diffusion equation (Eq. 16) that included both convective fluxes driven by J_v and molecular diffusion with effective diffusivity D_{LDL}^{w} (Table 2). At the endothelial surface, LDL flux was defined by the Kedem-Katchalsky formulation [49] (Eq. 17), accounting for both diffusive and convective contributions modulated by the selective permeability of the endothelium. Following the three-pore theory [47], the dominant LDL transport mechanisms were the leaky-junction and vesicular pathways, with the latter contributing approximately 10% of the leaky-junction flux (Eqs. 19–21).

Boundary conditions. For plasma, at the endothelium we impose the transwall flux J_v given in Eq. (4) (positive from lumen to wall). Across the IEL, hydraulic continuity is enforced:

$$J_{v,\text{IEL}}^{-} = J_{v,\text{IEL}}^{+} = L_{p,\text{IEL}}\,\Delta P_{\text{IEL}}, \qquad \Delta P_{\text{IEL}} = P_{\text{intima}} - P_{\text{media}}$$

At the EEL, a fixed extramural pressure is prescribed, $P = P_{\text{EEL}}$. For LDL, at the endothelium the convective-diffusive flux $J_{s,\text{LDL}}$ follows the Kedem-Katchalsky formulation (Eq. 17). Across the IEL, continuity of solute flux is enforced:

$$J_{s,\text{LDL,IEL}}^{-} = J_{s,\text{LDL,IEL}}^{+}$$

ensuring mass conservation between intima and media. At the EEL, a prescribed LDL concentration is imposed,

$$C_{\text{LDL}} = C_{\text{LDL}}^{\text{EEL}}$$

according to experimental data [50]. Within each layer, LDL oxidation is modeled as a first-order sink term:

$$R_{\text{LDL}} = -d_{\text{LDL}} C_{\text{LDL}}$$

where R_{LDL} represents the reactive sink term accounting for LDL oxidation, and d_{LDL} denotes the corresponding oxidation rate constant. All parameters used in the mass-transport model are summarized in Table 3.

2.5. Cellular dynamics (ABM)

The ABM represents cellular processes governing wall growth and remodeling driven by oxLDL and cytokine fields through a set of biologically inspired rules implemented in NetLogo 6.1 [58]. It operates

Table 2
LDL filtration and transport equations and relationships.

Definition	Equation	
LDL temporal evolution in the wall	$\frac{\partial C^w_{\mathrm{LDL}}}{\partial t} + \nabla \cdot \left(- D^w_{\mathrm{LDL}} \nabla C^w_{\mathrm{LDL}} \right) + k_{\mathrm{lag,LDL}}\, \mathbf{u}_p \cdot \nabla C^w_{\mathrm{LDL}} = f(\cdots, C^w_{\mathrm{LDL}}, \cdots)$	(16)
LDL flux across the endothelium (Kedem-Katchalsky)	$J_s = P_L\, \Delta C \left\{ \frac{Pe}{e^{Pe} - 1} \right\} + J_v\, (1 - \sigma_f)\, \bar{C}$	(17)
Peclet number	$Pe = \frac{J_v\, (1 - \sigma_f)}{P_L}$	(18)
Three-pore decomposition of LDL flux	$J_s = \cancel{J_{s,nj}} + J_{s,lj} + J_{s,vp}$	(19)
LDL flux through vesicular pathways	$J_{s,vp} = 0.1\, J_{s,lj}$	(20)
LDL flux through leaky junctions	$J_{s,lj} = P_{L,lj}\, \Delta C \left\{ \frac{Pe_{lj}}{e^{Pe_{lj}} - 1} \right\} + J_{v,lj}\, (1 - \sigma_{f,lj})\, \bar{C}$	(21)
Diffusive permeability of leaky junctions	$P_{L,lj} = \frac{D_{lj}}{\Delta x}\, \Phi_{lj}$	(22)
Effective diffusivity within leaky slits	$\frac{D_{lj}}{D_{\mathrm{free}}} = (1 - \alpha_{lj})(1 - 1.004\, \alpha_{lj} + 0.418\, \alpha^3_{lj} - 0.16\, \alpha^5_{lj})$	(23)
Steric hindrance ratio	$\alpha_{lj} = \frac{r_{\mathrm{LDL}}}{w_l}$	(24)
Assuming $C_l \gg C_w$ (simplified concentration gradient)	$\Delta C \approx C_l$	(25)

on a regular two-dimensional 300×300 lattice representing the cross-sectional geometry of the arterial wall, with each patch covering an area of 20×20 μm. This grid resolution was selected to match the characteristic length scale of individual vascular cells (on the order of tens of micrometers), enabling explicit single-cell representation and adequate resolution of intimal thickness while maintaining computational tractability for long-term simulations and repeated coupling with the transport model. Each lattice patch is classified either as lumen or as arterial wall, and wall patches are further labeled according to the tissue layer they represent (intima or media). Physiological interfaces (endothelium, IEL, and EEL) are encoded as barrier attributes on patches, reproducing layer-specific permeability.

Each lattice patch enforces single-occupancy constraints consistent with cell volume: ECs, FCs, and vSMCs are restricted to one cell per patch, whereas MCs may temporarily co-occupy a patch already containing another cell during phagocytosis to facilitate growth dynamics. The ABM follows a stochastic-deterministic formulation: continuous processes such as diffusion are described deterministically, whereas discrete cellular events (e.g., migration, proliferation, phenotype switching) are governed by probabilistic rules summarized in Table 4, where $p(x)$ denotes the probability of a cellular event occurring. Each rule includes quantitative parameters (migration probability, phagocytosis rate, cytokine secretion rate, ECM production rate, etc.) derived from experimental and literature data (Table 5).

Inputs and domain initialization. At the beginning of each ABM simulation, which spans a coupling interval of duration Δt_c, the oxLDL field computed by the mass-transport model is projected onto the ABM lattice via mesh-to-grid averaging and held constant as a quasi-static pro-inflammatory stimulus throughout Δt_c. Cytokines are generated by MCs during oxLDL phagocytosis and diffuse across the lattice according to an explicit 2D finite-difference scheme. The ECM density is a patch-level state variable updated at each step by sSMC-mediated ECM synthesis and by degradation arising from baseline turnover or MMP activity. Time advances in discrete steps ($\Delta t = 1$ day), with all agents and state variables updated at each iteration. This temporal resolution is consistent with the characteristic timescale of vascular cellular events (with a typical eukaryotic cell-cycle duration on the order of ~24 h [59]) and with established ABM formulations of early atherogenesis, in which agent attributes are updated on a daily basis [37,60,61].

Event logic and stochasticity. At each time step, the model updates: (i) the local oxLDL field; (ii) MCs dynamics—recruitment in response to excess oxLDL, lipid phagocytosis, cytokine secretion, and either lipid-overload transition to FCs or senescence-driven death upon a 100-day lifespan; (iii) vSMCs behavior—cSMC→sSMC switching, migration toward cytokine-rich regions, proliferation, apoptosis, and ECM synthesis; and (iv) ECM turnover (basal degradation and MMP-mediated degradation) and cytokine transport (decay and diffusion) (see Fig. 5).

Event triggering is probabilistic (Table 4). To map continuous local stimuli (e.g., oxLDL burden, or cytokine level) into bounded event probabilities, we adopt rule-specific sigmoidal response functions that impose saturation and limit event rates. In general form, the probability of an event driven by a stimulus X is defined as

$$P(X) = \frac{P_{\max}}{1 + e^{-k(X - X_{50})}} \tag{26}$$

where $P_{\max}$ defines the upper bound, X_{50} is the half-activation threshold, and k controls the sensitivity of the response around X_{50}. This formulation provides a smooth transition between basal and maximal activity, avoids discontinuities associated with step functions, and prevents unrealistically fast immune activation by ensuring bounded probabilities. Similar sigmoidal mappings have been used in ABM formulations of early atherogenesis and vascular adaptation [37,60,61].

Migration and remodeling algorithm. Cell migration and the local reorganization that follow cell proliferation were implemented through a modified A* search on the lattice [62] (see Fig. 6 which provides a simplified schematic example using 4-neighbour connectivity for illustration purposes only). A* is a graph-based path-finding algorithm that iteratively expands nodes by minimizing an evaluation function $f(n) = g(n) + h(n)$, where $g(n)$ is the accumulated cost from the origin, and $h(n)$ is a heuristic estimate of the remaining distance to the target. Lipid-rich necrotic core regions are treated as impassable obstacles. In our implementation, the domain corresponds to the discrete

Table 3
Parameters for plasma and LDL flow through the endothelium.

Parameter	Description	Value	Reference
Physical Properties			
k_{int}	Intima permeability	$2.2 \cdot 10^{-16}$ m^2	[51]
k_{med}	Media permeability	$2.0 \cdot 10^{-18}$ m^2	[51]
ϵ_{int}	Intima porosity	0.983	[51]
ϵ_{med}	Media porosity	0.258	[51]
$L_{p,snj}$	Normal junction conductivity	$2.0193 \cdot 10^{-8}$ $\frac{\text{cm}}{\text{s·mmHg}}$ *	[52]
μ_p	Plasma dynamic viscosity	0.001 Pa · s	[53]
ρ_p	Plasma density	1050 $\frac{\text{kg}}{\text{m}^3}$	[53]
D_{free}	LDL diffusion coeff. (free)	$1 \cdot 10^{-9}$ $\frac{\text{m}^2}{\text{s}}$	[54]
D_{LDL}	LDL diffusion coeff. (wall)	$5 \cdot 10^{-10}$ $\frac{\text{m}^2}{\text{s}}$	[28]
$k_{lag,\text{LDL}}$	Solute lag coefficient of LDL	0.893	[54]
d_{LDL}	LDL oxidation rate	$2.85 \cdot 10^{-4}$ s^{-1}	[51]
Dimensions			
A_{unit}	Unit area	0.64 mm^2	[29]
l_{ij}	Length of a leaky junction	2 μm	[55]
R_{cell}	Endothelial cell radius	15 μm	[55]
w_l	Half-width of a leaky junction	20 nm	[55]
r_{LDL}	LDL radius	11 nm	[56]
Pressures			
P_{EEL}	Pressure at the EEL	30 mmHg	[51]
ΔP_{end}	Pressure drop in the endothelium	21.6364 mmHg**	[52]
Concentrations			
C^{l}_{LDL}	LDL concentration in the lumen	4.914 $\frac{\text{mol}}{\text{m}^3}$	[57]
$C^{\text{EEL}}_{\text{LDL}}$	LDL concentration at the EEL	0.0678 $\frac{\text{mol}}{\text{m}^3}$	[50]

* The value of the parameter is dependent on the considered artery (Table value for coronary arteries).
** The value of the parameter is dependent on the intraluminal pressure (Table value of 110 mmHg).

Table 4
Summary of ABM rules governing cellular behavior. Deterministic rules compute concentration changes, while stochastic rules determine event probabilities using sigmoid functions.

Agent	Event	Rule
Monocytes/MCs	Recruitment and differentiation	$p_{\text{produce}_{MC}} = \frac{m_d}{1 + e^{-k\left(C_{\text{oxLDL}} - C_{\text{oxLDL}_0}\right)}}$
	Phagocytosis of oxLDL and cytokine secretion	$\begin{cases} \text{oxLDL}^{t}_{MC} = \text{oxLDL}^{(t-1)}_{MC} + r_{\text{phago}}\, \text{oxLDL}^{(t-1)}_{\text{patch}} \\ \text{cyto}^{t} = \text{cyto}^{(t-1)} + r_{\text{secr}_{\text{cyto}}}\, \text{oxLDL}^{(t-1)}_{\text{patch}} \end{cases}$
	FC transition	if $\text{oxLDL}_{MC} > \text{oxLDL}_{MC_{\max}} \Rightarrow \begin{cases} \text{release MMPs} \\ \text{switch to FC} \end{cases}$
	Death	if $t_{\text{life}} > t_{\text{lifespan}} \rightarrow$ die
vSMCs	Phenotypic switching (cSMC → sSMC)	$p_{\text{diff}} = \frac{r_{\text{diff}}}{1 + e^{-(C_{\text{cyto}} - C_{\text{cyto}_0}) + d}}$
	sSMC Proliferation	$p_{\text{prolif}} = \frac{r_{\text{prolif}}}{1 + e^{-(C_{\text{cyto}} - C_{\text{cyto}_0}) + d}}$
	sSMC Migration	$p_{\text{migrate}} = \frac{1}{1 + e^{-(C_{\text{cyto}} - C_{\text{cyto}_0}) + d}}$
	sSMC Apoptosis	$p_{\text{apop}} = r_{\text{apop}}$
	sSMC ECM production	$\text{ECM}^{t} = \text{ECM}^{t-1} + r_{\text{gen}_{\text{ECM}}}$

arterial wall, discretized with 8-neighbour connectivity and step costs of 1 (orthogonal) or $\sqrt{2}$ (diagonal). Using this algorithm to compute the shortest path is consistent with the minimum-energy principle described by [63], in which cells choose trajectories that minimize the energy required to reach their target (i.e., to drive tissue remodeling). We further modified this path-finding algorithm by incorporating the influence of the ECM into the cost function, thereby mimicking how cells mechanosense their surroundings to decide which trajectory to follow. This ECM-dependent term was conceived as a mechanistically motivated proxy for the local resistance imposed by the extracellular environment during tissue reorganization. Experimental studies indicate that cell migration depends on local matrix stiffness gradients, ECM composition, collagen density, pore structure, and confinement, all of which can affect migration speed and directional bias [64,65]. Accordingly, regions with higher ECM density were assumed to be less permissive and were therefore assigned a higher migration/remodeling cost. Consequently, newly generated or migrating sSMCs tend to select less resistant and therefore energetically favorable routes toward an admissible site.

Coupling time. To ensure consistency with the temporal resolution of the BIOCCORA porcine dataset and the faster dynamics of plaque evolution in this model, we set a single coupling interval of nine months. In our previous human-based framework, multi-year coupling was sufficient given the slower progression of atherosclerosis [41]. However, in pigs under a high-fat diet, plaque remodeling occurs within a much shorter timescale. The nine-month interval was chosen because (i) it corresponds to the second imaging time point (T2) available in the study, enabling data-anchored model updates and validation, and (ii) some

Table 5
Global ABM parameters.

Parameter	Description	Value	Reference
r_{diff} (d^{-1})	Differentiation rate from cSMCs to sSMCs	1	[30]
r_{prolif} (d^{-1})	Proliferation rate	0.24	[66]
r_{apop} (d^{-1})	Apoptosis rate	1.9008×10^{-5}	[67]
$r_{gen_{ECM}}$ (d^{-1})	ECM generation rate	2.1384×10^{-16}	[68]
$r_{deg_{ECM}}$ (d^{-1})	ECM degradation rate	1/30	–
C_{mono_blood} (mol/m^3)	Monocytes in blood	550×10^{9}	[69]
m_r (d^{-1})	Monocyte recruitment rate	6.636×10^{-4}	[70]
m_d (d^{-1})	Monocyte differentiation rate	9.94×10^{-2}	[28,71]
$r_{secr_{cyto}}$ (d^{-1})	Secretion rate of cytokines	2.592×10^{-5}	[28]
$r_{deg_{cyto}}$ (d^{-1})	Degradation rate of cytokines	2	[28,72]
$r_{secr_{MMPs}}$ (d^{-1})	Secretion rate of MMPs	2.592×10^{-6}	–
$r_{deg_{MMPs}}$ (d^{-1})	Degradation rate of MMPs	2	–
$oxLDL_{MC_{max}}$ (mol)	Maximum phagocytic capacity	6.7×10^{-15}	–
r_{phago} (d^{-1})	Phagocytosis rate	2.1168×10^{-18}	–

animals did not reach the 12-month follow-up, making earlier couplings (e.g., at six months) unsupported by imaging data and potentially unreliable. Accordingly, this validation study used the baseline (T1) 3D reconstruction as a fixed CFD domain and applied a sequential coupling (CFD → transport → ABM) without 3D remeshing. This setup thus provided a realistic temporal synchronization between simulated and experimental plaque development.

Parameter calibration. Model calibration was performed to adjust the agent-based rules governing oxLDL phagocytosis and maximum MC uptake capacity, which were considered the most directly linked to the accelerated porcine progression rate. All other rules and parameters were retained unchanged, so that the underlying mechanobiological structure of the model remained consistent with the human-based framework.

Calibration was conducted through a structured iterative manual procedure guided by quantitative agreement between simulations and experimental observations. A fully automated optimization algorithm was not implemented due to the hybrid architecture of the framework, which couples 3D CFD, 2D mass transport, and ABM modules executed across two different software environments, with substantial computational cost per simulation. Under these conditions, a manual calibration strategy was considered methodologically appropriate and computationally feasible.

First, the model was run on a representative coronary geometry from the porcine dataset (Pig #1-LAD), using baseline parameters [41] as initial estimates. Second, the parameters controlling MC activity were progressively adjusted to reduce the discrepancy between simulated and experimental ΔWT and SR at nine months. In addition to matching these continuous metrics, the presence or absence of lipid-pool formation was used as a qualitative consistency criterion to ensure that the model reproduced the observed plaque phenotype.

Calibration runs were executed using ten stochastic simulations per parameter set to account for the probabilistic nature of the ABM. The average response was compared with the experimental trends, and the parameter set yielding the lowest error was retained (see Section 3.1).

2.6. Validation strategy

After calibration on the Pig #1–LAD artery, the model was evaluated on the remaining three coronary arteries selected from the BIOCCORA dataset (Pig #1–RCA and Pig #2–LAD/RCA). This ensured that validation was performed on vessels not used during calibration, thereby providing an independent assessment of the model's predictive ability.

The validation was performed by comparing model predictions at T2 with experimental measurements obtained at that same time point, using T1 as the baseline geometry. In this context, validation is defined as the model's ability to reproduce key geometric and biological features of plaque progression observed in vivo. Specifically, we evaluated the model's accuracy through the following steps:

- Qualitative comparison. We performed a qualitative evaluation by comparing simulated plaque progression with OCT-based contours for different cross-sections. This included assessing overall plaque morphology, eccentric growth patterns, and lipid-rich necrotic core formation across different TAWSS levels, ensuring that the model captures the key spatial trends observed experimentally.
- Quantification of SR, computed as the relative reduction in lumen area with respect to the baseline geometry, and compared between the simulated and experimental results. SR was analyzed at three representative cross-sections (CS1-CS3) per artery, each corresponding to regions of high, intermediate, and low TAWSS. This targeted approach enables a direct comparison between the model and experiment across the distinct hemodynamic environments that drive heterogeneous plaque evolution.
- Quantitative assessment of ΔWT, defined as the change over time (from T1 to T2) in the radial distance between the lumen and the EEL, measured at corresponding angular positions and compared between the model and the OCT-derived contours. Angular correspondence was ensured by aligning the IVUS/OCT cross-sections with the centerline used for model input, maintaining consistent angular references during both segmentation and simulation.

Together, these validation steps aim to assess the model's qualitative and quantitative ability to predict plaque morphology, composition, and growth patterns. The entire computational pipeline required about eight hours per artery on a workstation with an Intel(R) Core(TM) i7-10700K CPU @ 3.80GHz (8 cores/16 threads). This computational time includes the full workflow: post-processing of 3D CFD simulations, 2D LDL/oxLDL mass-transport analyses, and execution of the ABM across the selected cross-sections over the nine-month progression.

2.7. Statistical analysis

Here, we performed a statistical comparison between simulated outputs and experimental measurements across all analyzed cross-sections to evaluate the consistency of model predictions with experimental data. To assess the model's predictive capabilities, we separated the dataset into a calibration set (Pig #1–LAD) and an independent validation set (Pig #1–RCA, Pig #2–LAD, and Pig #2–RCA). For SR, we compared simulated outputs across 50 coronary cross-sections for the calibration artery ($n = 50$) and 50 cross-sections for each of the three validation arteries (total validation $n = 150$).

For ΔWT, we evaluated the agreement between simulations and experiments using a sector-level database. Each of the 50 cross-sections per artery was partitioned into 8 circumferential sectors, yielding $n = 400$ sectors for the calibration set and $n = 1200$ sectors for the independent validation set. Sector values were stratified into TAWSS tertiles (low, medium, high). For both SR and ΔWT, we computed the global mean bias (Sim-Exp) and the Mean Absolute Error (MAE) separately for the calibration and validation sets. Paired agreement was assessed using the two-sided Wilcoxon signed-rank test, appropriate for non-normal paired differences; statistical significance was set at $p < 0.05$.

All statistical computations and visualizations were performed in Python 3.10 using `pandas` and `scipy`.

3. Results

This section presents the outcomes of the multi-level validation designed to assess the predictive performance of the hybrid model. Results are structured following the validation strategy described in Section 2. First, we summarize the parameter calibration procedure. Second, we provide a qualitative assessment of plaque progression by comparing simulated geometries with OCT-based reconstructions, focusing on spatial patterns of growth relative to TAWSS. Next, we quantify model performance for both SR and ΔWT. Representative SR comparisons are

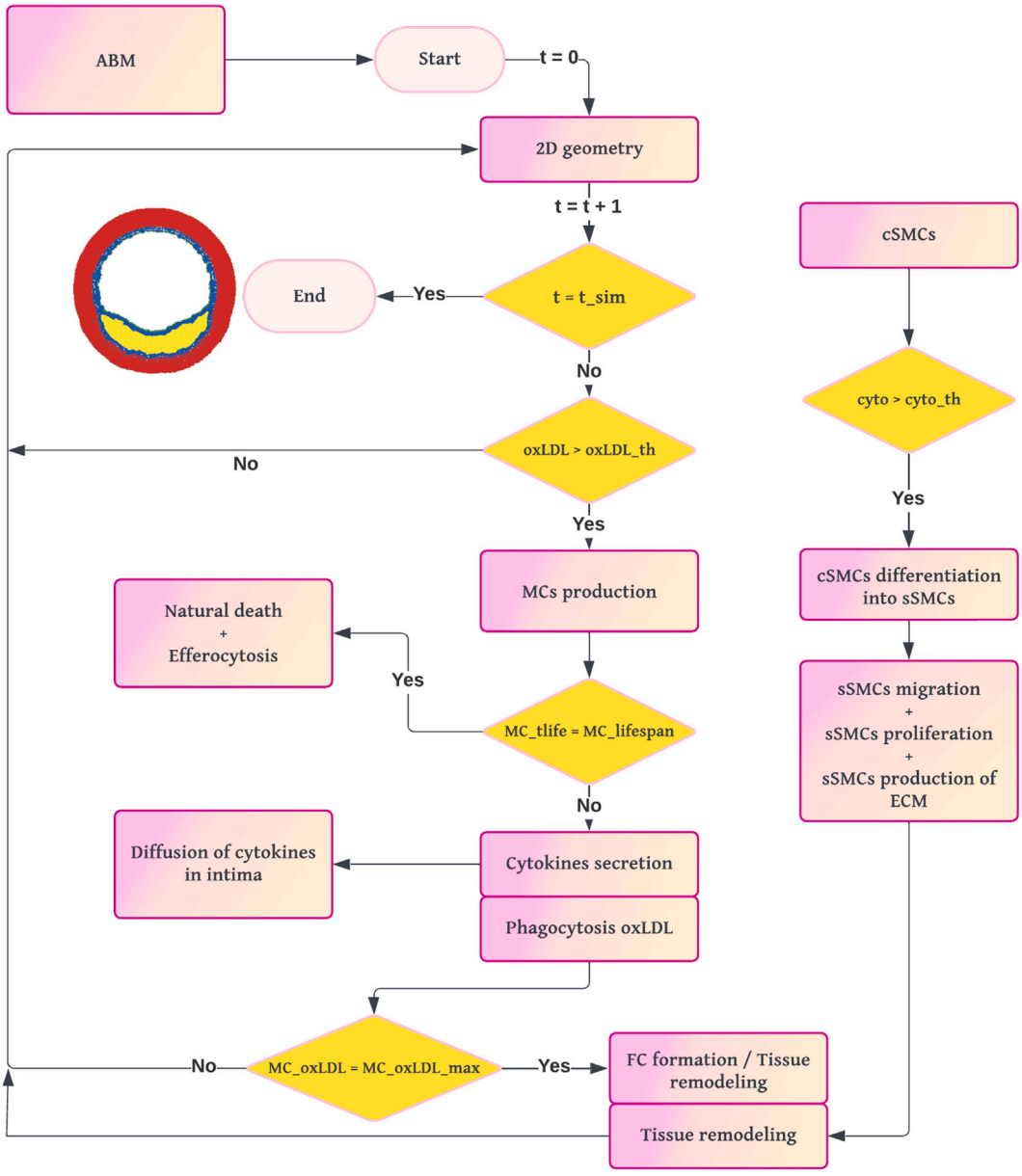

Fig. 5. Workflow diagram of the ABM. The process begins with the 2D cross-section from the mass transport model. For each loop until the simulation time of the ABM is reached, if there is a pathological concentration of oxLDL, the model computes the probability of production of MCs and their dynamics. The formation of FCs leads to the appearance of a lipid-rich necrotic core, and the secretion of cytokines triggers the vSMC activity.

shown for selected cross-sections, whereas the global statistical assessment is based on all analyzed sections (and all sector-level measurements for ΔWT). Finally, we report the results of the statistical analyses evaluating the global agreement and the consistency of global trends. For clarity, results are organized by pig. Figs. 7, Fig. 9(A) and (B), and Fig. 10(A) and (B) summarize the validation results for pig #1, while Figs. 8 and 9(C) and (D), and Fig. 10(C) and (D) correspond to pig #2.

3.1. Calibration results

The final calibrated parameters for MC dynamics are summarized in Table 6. Compared with the original human-based configuration, the porcine calibration required a higher phagocytosis rate and a reduced maximum phagocytic capacity, reflecting the faster lipid turnover and plaque expansion observed experimentally. These adjustments preserved a consistent ratio between the amount of oxLDL internalized per MC and the temporal scale of the phagocytic process, ensuring biological plausibility.

Fig. 7(A) illustrates the qualitative comparison between simulated plaque progression and OCT data. In CS1 (high TAWSS), both the experiment and simulation indicated negligible growth, consistent with the protective role of elevated shear stress. CS2 (intermediate TAWSS) displayed moderate thickening, which the model reproduced, although with a slight overestimation. In CS3 (low TAWSS), the simulation captured pronounced eccentric growth and the formation of a necrotic lipid-rich plaque, closely matching the experimental lipid distribution after 270 days. Both CS2 and CS3 exhibited inward and outward remodeling, in agreement with the Glagov phenomenon [14].

Quantitatively, SR analysis for the three representative sections (Fig. 9(A)) confirmed these trends: errors were minimal in CS1 (≈2%) and CS2 (≈2%), and higher in CS3 (14.8%). The overall accuracy metric for this artery was MAE = 6.24%. These results suggest that most of the mismatch stems from the reconstruction of lipid cores in low-TAWSS regions.

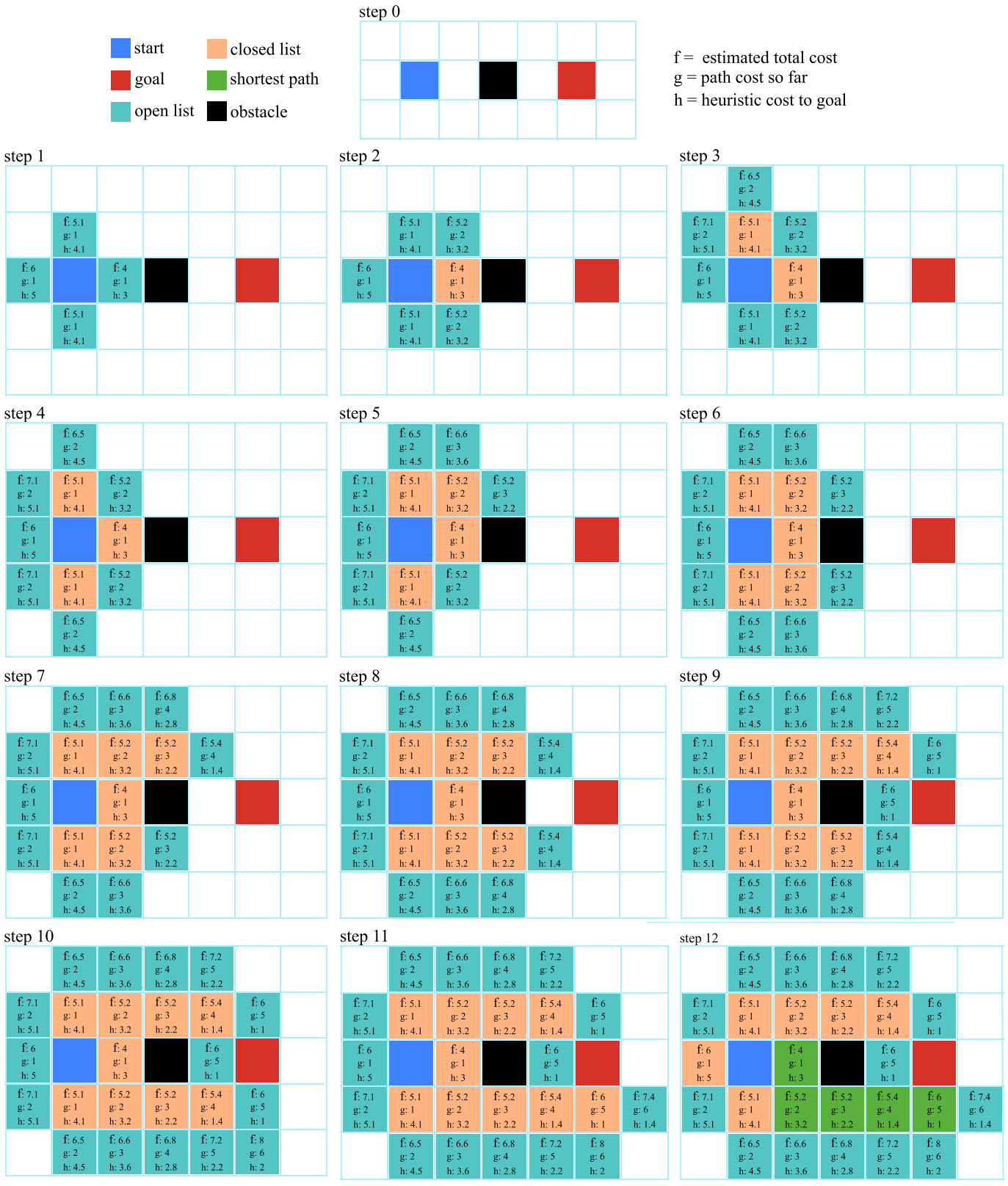

Fig. 6. Simplified grid-based A* search with an obstacle. The domain is a 2D lattice with 4-neighbour connectivity (no diagonals) and a unit step cost. This figure is provided as a schematic illustration only; in the full ABM implementation, the arterial wall lattice uses 8-neighbour connectivity, with step costs of 1 (orthogonal) and $\sqrt{2}$ (diagonal), as described in the main text. The heuristic h corresponds to the Euclidean distance to the goal. For each node, g denotes the accumulated cost from the start, h the estimated remaining cost to the goal, and $f = g + h$ the evaluation function minimized by the A* algorithm. Colors: start (blue), goal (red), open set (cyan), closed set (amber), and final path (green); obstacle cells (black) are impassable. Labels on selected nodes show their respective g, h, and f values. The obstacle forces a detour, and the goal is reached after twelve node expansions.

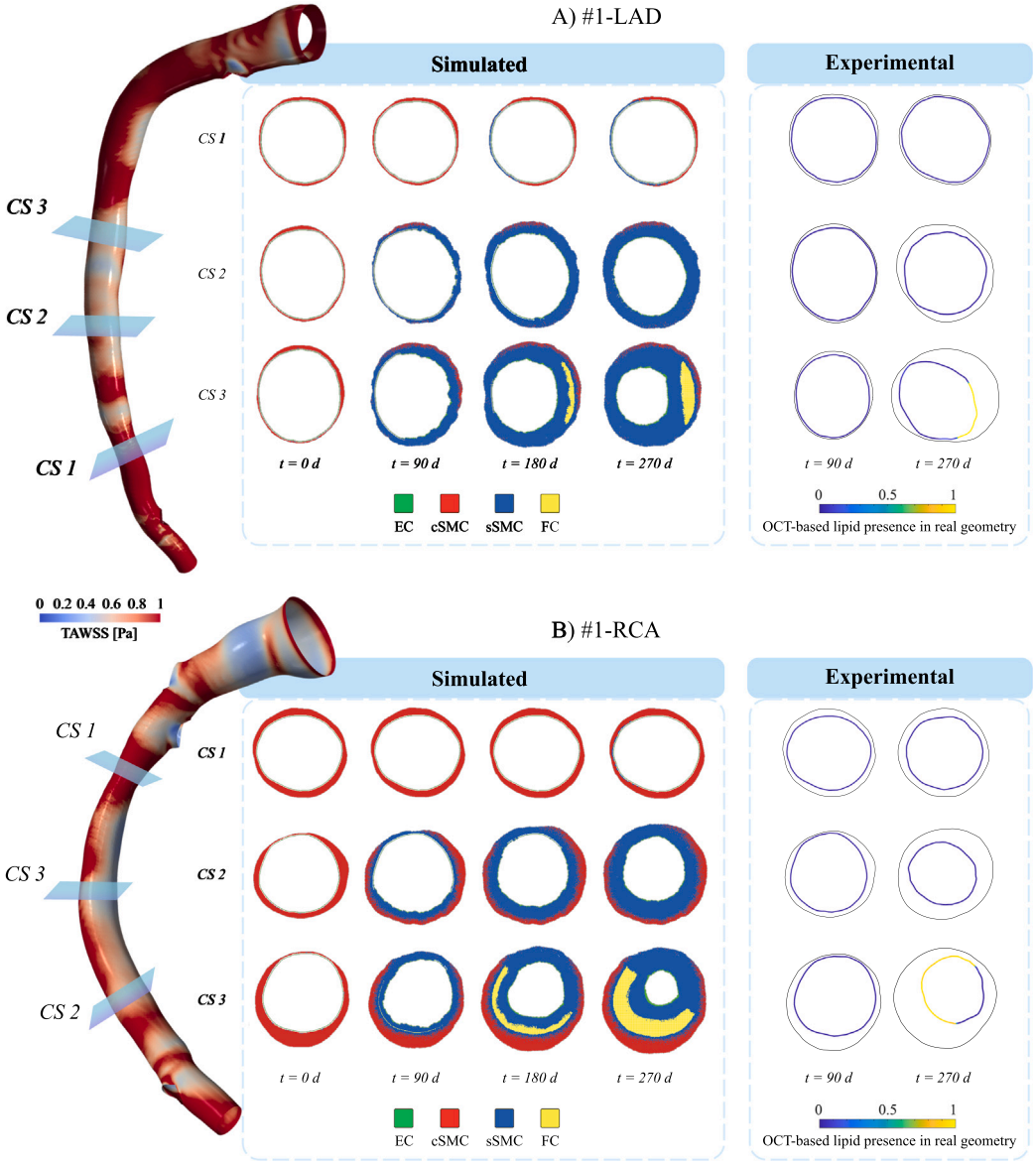

Fig. 7. Qualitative comparison of simulated plaque progression in pig #1. (A) LAD and (B) RCA. Baseline geometry is color-coded by TAWSS (saturated at 1 Pa). Three representative cross-sections (CS1–CS3) illustrate regions of high, intermediate, and low TAWSS exposure. Simulated temporal evolution ($t = 0, 90, 180, 270$ days) is compared with OCT-derived measurements at $t = 90, 270$ days.

The sector-based evaluation of wall-thickness variation (Fig. 10(A)) reinforced these findings. The model reproduced the magnitude and spatial variability of ΔWT with good agreement, successfully capturing the overall trend (MAE = 0.091 mm), which corresponds to approximately 4–5 ABM grid cells (patch size: 20 μm) and remains well below the experimentally observed thickening in low-TAWSS sectors (typically ~0.20–0.25 mm over 9 months). Moreover, this error magnitude is on the order of the axial resolution of IVUS, indicating that discrepancies approach the intrinsic measurement limits of the validation data.

3.2. Validation results

3.2.1. Pig #1

RCA artery. Fig. 7(B) shows the qualitative comparison for the RCA. In CS1, located in a high-TAWSS sector, the model predicted no growth, similar to the experimental outcomes, and consistent with the protective effect of elevated shear stress. In CS2, under intermediate TAWSS, the simulation predicted moderate progression, in close agreement with the experimental contours. In CS3, exposed to low TAWSS, the model reproduced plaque formation and lipid accumulation, aligning with OCT data, but slightly overestimated the extent of lipid-rich regions. Importantly, asymmetric growth localized to the low-TAWSS side of the circumference was accurately captured by the model.

Quantitative SR analysis (Fig. 9(B) showed errors of ≈2% in CS1, 22.6% in CS2, and 20.7% in CS3, yielding an overall MAE of 15.10%. In CS1, the prediction is in very close agreement with the experimental data: minimal growth was expected under high TAWSS and was accurately reproduced by the model. By contrast, CS2 and CS3 exhibited larger discrepancies, indicating that although the model captures the direction of disease progression, quantitative prediction of lumen narrowing remains more challenging in more developed lesions. In CS2, the experimental SR at intermediate TAWSS exceeds the simulated value, while the ΔWT prediction is in good agreement (Fig. 10(B), consistent with negative remodeling—i.e., concurrent luminal narrowing not driven by wall thickness growth—thereby elevating SR without a

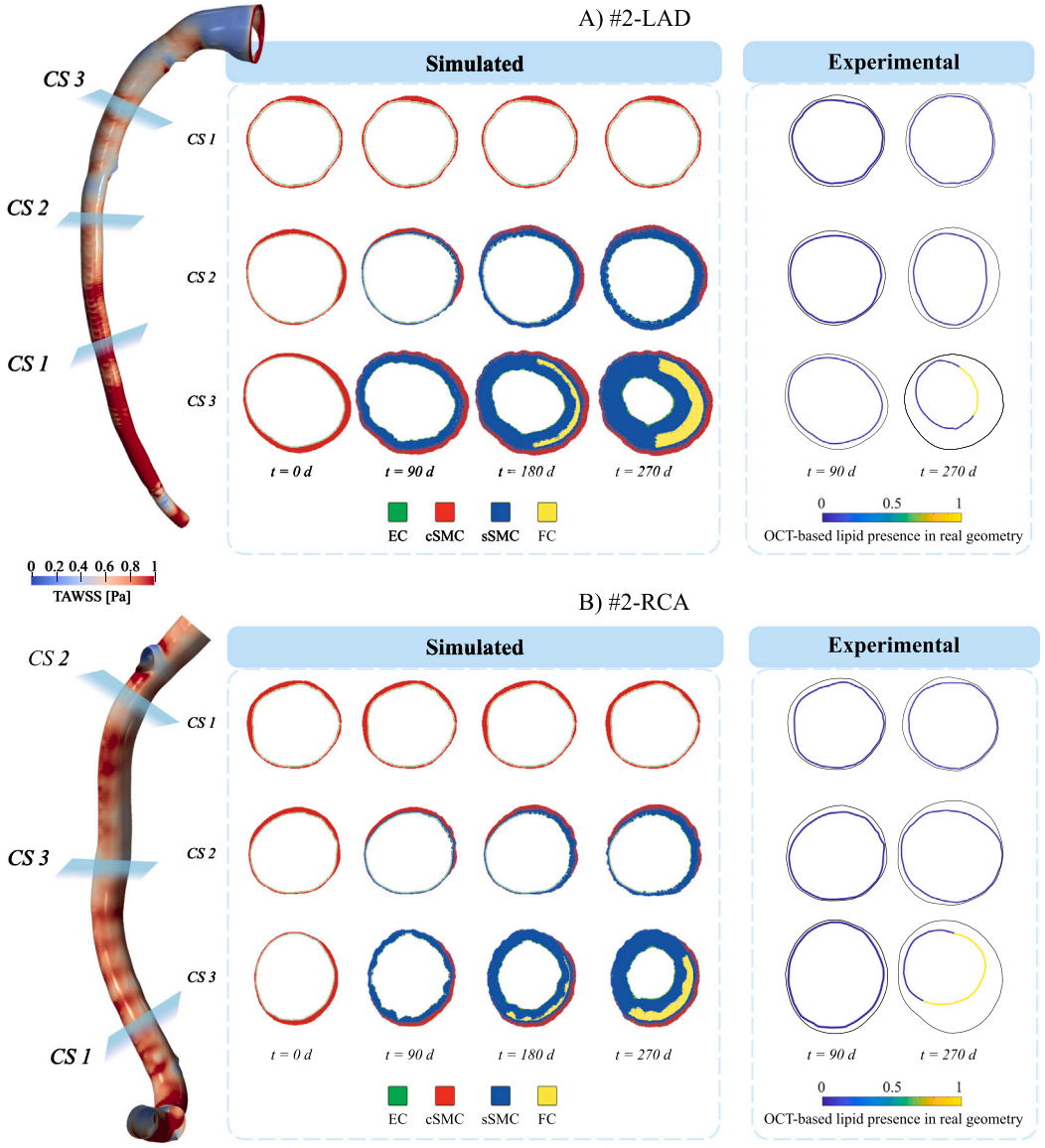

Fig. 8. Qualitative comparison of simulated plaque progression in pig #2. (A) LAD and (B) RCA. Baseline geometry is color-coded by TAWSS (saturated at 1 Pa). Three representative cross-sections (CS1-CS3) illustrate regions of high, intermediate, and low TAWSS exposure. Simulated temporal evolution ($t = 0, 90, 180, 270$ days) is compared with OCT-derived measurements at $t = 90, 270$ days.

notable increase in ΔWT. In CS3, the discrepancy is consistent with a systematic bias stemming from the lack of quantitative experimental data on necrotic core morphology. Since the experimental dataset only provided binary information regarding lipid presence, the volumetric growth and mechanical expansion of the simulated necrotic core are numerically unconstrained during calibration. This may lead to an overestimation of inward remodeling toward the lumen, thereby inflating the SR estimates in sections where lipid-rich regions are prominent. Despite these local deviations, the ΔWT comparison showed good overall agreement (MAE = 0.159 mm), with residual mismatches largely attributable to growth overestimation in CS3, while the global trend was captured.

3.2.2. *Pig #2*

LAD artery. Fig. 8(A) illustrates the results for the LAD artery of pig #2. In CS1 (high TAWSS), both simulation and experiment showed negligible changes, with excellent agreement. CS2, exposed to medium-low TAWSS, exhibited moderate thickening, closely reproduced by the model. In CS3, located in a low-TAWSS region, the simulation predicted marked wall thickening and lipid accumulation, consistent with OCT data, although the extent of progression was overestimated. In this case, the model detected asymmetric growth, but it was less pronounced than in the experimental observation. Moreover, the circumferential plaque growth was slightly overestimated.

Quantitative SR comparison (Fig. 9(C)) revealed errors of 3.0% in CS1, 2.0% in CS2, and 26.0% in CS3. The overall MAE was 10.33%. The error in CS3 was higher probably due to the overestimation of plaque formation. Wall thickness analysis (Fig. 10(C)) supported these observations, showing that the model reproduced the spatial distribution of thickening with a global MAE of 0.123 mm and correctly localized the maximum ΔWT to the low-TAWSS region. In addition, the difference between experimental and simulated ΔWT in the low-TAWSS group was moderately small, in contrast to the discrepancies observed in SR predictions. This points to a generally good agreement for wall growth.

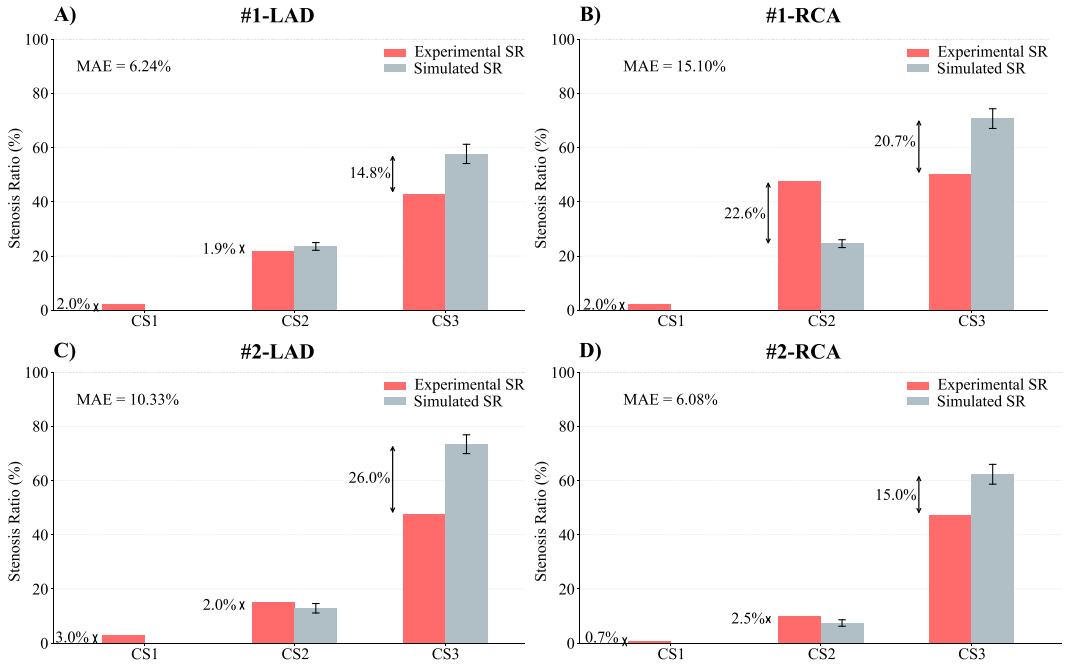

Fig. 9. Quantitative comparison of SR between experimental measurements (red) and model predictions (gray) at the three representative cross-sections (CS1–CS3) selected for each artery. Gray bars represent the mean simulated SR across repeated stochastic ABM realizations, and error bars indicate the corresponding standard deviation. Panels correspond to: (A) #1-LAD, (B) #1-RCA, (C) #2-LAD, (D) #2-RCA. Black arrows indicate the absolute difference between the mean simulated and experimental SR. MAE is reported for each artery.

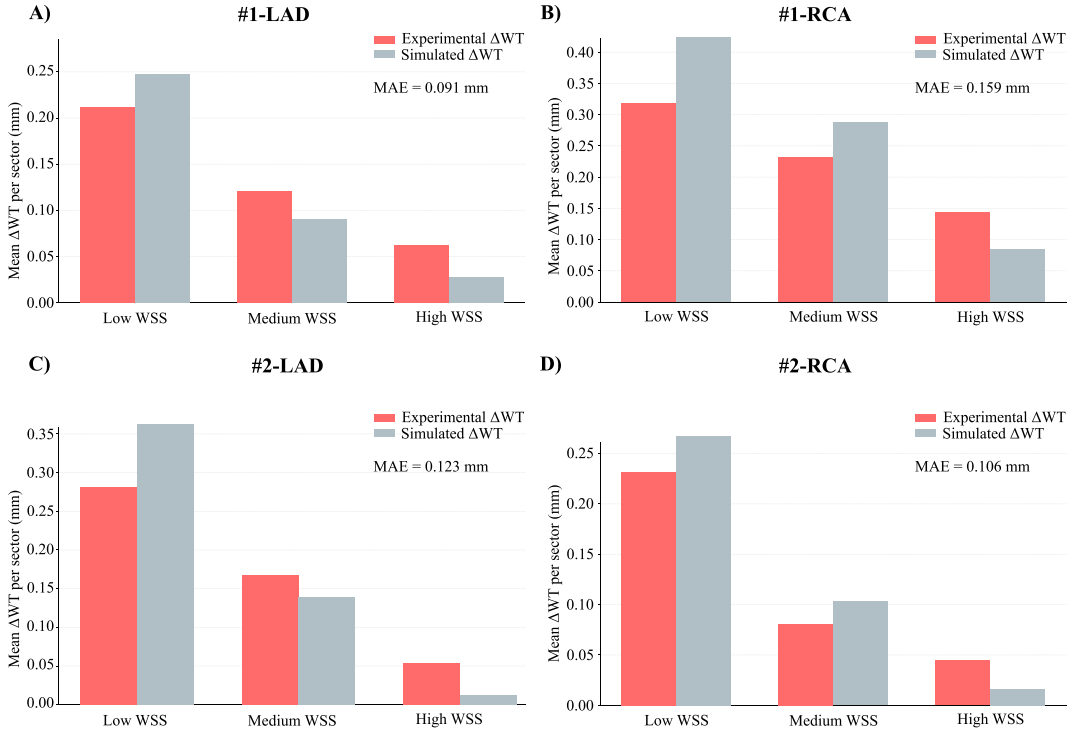

Fig. 10. Quantitative comparison of wall thickness variation (ΔWT) between experimental measurements (red) and model predictions (gray) across all the sectors stratified into TAWSS tertiles (low, medium and high). Panels correspond to: (A) #1-LAD, (B) #1-RCA, (C) #2-LAD, (D) #2-RCA. MAE is reported for each artery.

RCA artery. The qualitative comparison for the RCA (Fig. 8(B)) showed stable conditions in CS1 (high TAWSS), with no detectable progression in either the experiment or the simulation. CS2 (intermediate TAWSS) exhibited moderate wall thickening that the model reproduced with good accuracy. In CS3 (low TAWSS), both the model and the experiment revealed extensive plaque progression and lipid accumulation.

Table 6
Calibrated parameters for MC dynamics in the porcine BIOCCORA dataset.

Parameter	Human calibration	Porcine calibration
Maximum phagocytic capacity ($oxLDL_{MC_{max}}$)	6.7×10^{-15} mol	3.1×10^{-15} mol
Phagocytosis rate (r_{phago})	2.1×10^{-18} d^{-1}	30×10^{-18} d^{-1}

Table 7
Error metrics (bias and MAE) and Wilcoxon signed-rank test results for simulated vs experimental SR and ΔWT. Bias is reported as (Sim–Exp). Results are separated into the calibration case (Pig #1–LAD) and the independent validation set (pooled across Pig #1–RCA, Pig #2–LAD, and Pig #2–RCA).

Metric	Set	n	Bias	MAE	p-value
SR (%)	Calibration	50	+1.98	12.7	0.461
SR (%)	Validation	150	+1.41	15.6	0.431
ΔWT (mm)	Calibration	400	−0.02	0.09	0.336
ΔWT (mm)	Validation	1200	−0.05	0.13	0.501

Quantitative SR analysis (Fig. 9(D) confirmed this behavior, with very small errors in CS1 (<1%) and CS2 (2.5%), and a moderate error in CS3 (15.0%). However, the discrepancy in CS3 is not negligible. While the experimental lesion developed eccentrically, the simulated growth followed a more concentric pattern, thereby underestimating the lesion's asymmetry and the resulting luminal narrowing. This underestimation of asymmetry is a natural limitation when the local hemodynamic triggers are relatively uniform circumferentially, leading the model to distribute wall thickening more evenly than in the biological reality. Global performance was the best among all arteries, with MAE = 6.1%. Predictions of ΔWT (Fig. 10(D)) also demonstrated excellent agreement with experimental data in both magnitude and spatial distribution, showing a MAE of 0.106 mm.

3.3. Statistical analysis

The results of the statistical analysis are summarized in Table 7. For SR within the validation set, the model showed a generally good agreement with experimental measurements. The validation bias was slight (+1.41%), and errors remained reasonably low (MAE = 15.6%). As expected, the calibration set exhibited a lower MAE (12.7%) because global model parameters were tuned using this geometry; its slightly higher bias (+1.98%) is likely influenced by the fact that calibration relies on a single vessel, whereas the validation metrics reflect pooled behavior across three independent arteries. In general, the model tended to slightly overestimate SR at higher stenosis levels and slightly underestimate it at lower ones, while maintaining errors that remain well contained and acceptable for this type of analysis. The Wilcoxon test confirmed no significant paired bias in the validation set (p-value = 0.431), consistent with the small mean difference (+1.41%). Overall, the model captures the key trends of SR progression and reliably identifies regions prone to lumen narrowing, but cases of pronounced growth still require refinement.

For ΔWT, the agreement in the validation set was stronger, with minimal bias (−0.05 mm), and moderately low errors (MAE = 0.13 mm). Consistent with the SR evaluation, the calibration MAE for ΔWT was lower (0.09 mm), reflecting the expected fit performance on the calibration artery, while the independent validation results remained comparable in magnitude. Importantly, paired statistical testing revealed no significant difference between simulated and experimental ΔWT values for the validation cases (p-value = 0.501).

4. Discussion

This validation study confirms that our multiscale hybrid model—coupling CFD, mass transport, and agent-based dynamics—captures the essential features of atherosclerotic plaque evolution observed in the BIOCCORA porcine dataset. Across the four arteries analyzed, the model consistently reproduced the expected phenotypes by hemodynamic exposure, including eccentric thickening and lipid-rich regions localized to low-TAWSS sectors. In line with pathophysiological mechanisms, our framework converted TAWSS into spatially localized wall remodeling in atheroprone regions [15,16,20,22]. Key observations reinforce the biological plausibility of the model: low-TAWSS sectors preferentially developed wall thickening and lipid accumulation, whereas high-TAWSS sectors remained comparatively protected.

The emergence of both outward and inward remodeling, in agreement with the Glagov phenomenon [14], illustrates the ability of the framework to reproduce emergent behaviors that were not hard-coded but arose naturally from the coupled biophysical and cellular rules. Specifically, this remodeling behavior is a consequence of the A*-based tissue reorganization used in the model. When new plaque-related mass is generated, the algorithm relocates cells by seeking the lowest-cost free path, where the path cost combines distance with an ECM-dependent penalty. In early stages, many newly formed sSMCs arise radially outside the growing lipid-pool, and the lowest-cost relocation path typically points toward the exterior, promoting expansion of the outer wall rather than immediate luminal encroachment. As sSMCs progressively occupy positions closer to the lumen, the lowest-cost available paths more frequently connect to the interior, and inward remodeling becomes more prevalent. This mechanism thereby provides a plausible explanation for the transition from compensatory enlargement to luminal narrowing.

Predictions of SR reproduced the expected spatial trends and TAWSS hierarchy across arteries. Localized but non-negligible SR discrepancies nevertheless remained in a subset of advanced cross-sections. Because SR jointly reflects wall thickening and lumen remodeling, it may deviate even when ΔWT is reasonably reproduced. The largest mismatches were concentrated in low-TAWSS, lipid-rich, highly eccentric lesions, where the experimental dataset provided lipid information only as a binary OCT-based presence/absence feature rather than as a quantitative reconstruction of lipid-core geometry or burden. This limits calibration and validation of the modeled necrotic core in advanced plaques. In addition, cross-sections undergoing negative remodeling may exhibit substantial lumen reduction without a proportional increase in ΔWT, thereby increasing SR while preserving relatively good agreement in wall-thickness predictions. Beyond these localized discrepancies, qualitative comparisons showed good alignment with the distribution of lipid-rich regions and with the overall patterns of wall growth and remodeling. Agreement in ΔWT further supports the mechanobiological consistency of the framework, through the explicit representation of endothelial permeability, macrophage activation, vSMC phenotypic switching and migration, hyperplasia, and lipid-core development. In this context, the global ΔWT error magnitude (MAE = 0.13 mm) remains consistent with a quantitatively accurate sector-level description of wall remodeling. The statistical analysis further corroborated that the model distinguished atheroprone from atheroprotective scenarios according to TAWSS.

Hybrid multiscale frameworks are increasingly used in vascular modeling because plaque evolution arises from tightly coupled mechanisms acting across scales. Compared with studies relying exclusively on CFD-derived inflammation [40], our framework extends predictive capacity by incorporating downstream biological processes and geometric feedback. While continuum growth and remodeling models have successfully reproduced remodeling patterns at larger scales [73,74], they provide powerful tools to describe arterial adaptation through constitutive evolution laws, often under homogenized material assumptions and without explicitly incorporating cellular-level mechanisms. In contrast, agent-based approaches in the literature have largely focused on simplified vascular geometries or early lesion stages [60]. By integrating ABM with CFD and mass transport in a temporally coupled loop, our framework bridges these approaches. A recent hybrid framework has similarly coupled CFD, LDL transport, and ABM-based cellular dynamics in the context of atherosclerosis [42], representing

an important and complementary advance in multiscale modeling of coronary plaque progression. A structured comparison along the main methodological axes helps to delineate the specific contributions of each study. Regarding the CFD strategy, both frameworks employ transient simulations with patient- or subject-specific Doppler-derived boundary conditions and model blood as a Newtonian fluid. The present work used pre-computed CFD outputs from the BIOCCORA study on porcine geometries, while [42] performed CFD directly on a single human LAD artery reconstructed from CCTA and IVUS data. The LDL transport formulations differ more substantially. The present framework employs a 2D multi-layer convection-diffusion-reaction model of intramural transport, resolving LDL and oxLDL concentration fields within the wall layers (intima and media) via Darcy flow and Kedem-Katchalsky endothelial filtration, with oxLDL explicitly tracked as the pro-inflammatory trigger. In contrast, [42] adopt a wall-free 3D advection-diffusion model for luminal LDL polarization, coupled to a three-pore model that computes the trans-endothelial LDL flux as a scalar input to the ABM, without resolving intramural transport or oxidation. Both approaches share the three-pore framework for endothelial permeability, but differ in whether intramural dynamics are explicitly resolved. Regarding ABM implementation, both models operate on 2D cross-sectional lattices and represent SMC and ECM dynamics. The present framework additionally tracks macrophage recruitment, oxLDL phagocytosis, foam cell formation, and cytokine-mediated signaling as explicit agents, with an A*-based tissue reorganization algorithm that incorporates ECM-dependent migration costs. The ABM in [42] represents lipid infiltration probabilistically as a function of LDL influx, and SMC and ECM dynamics as functions of WSS and a Gaussian-based inflammatory input, without explicitly modeling macrophage agents or foam cell formation. Finally, the validation strategies reflect different but complementary objectives. [42] performed the first proof-of-concept patient-specific validation in a human LAD artery, comparing wall area variation at three cross-sections against IVUS data at one-year follow-up. The present study adopts a different design, evaluating the framework across four porcine coronary arteries using longitudinal IVUS and OCT data over nine months, with sector-level assessment of both SR and ΔWT stratified by TAWSS tertiles. This controlled preclinical setting enables access to early phases of plaque initiation that are difficult to capture prospectively in human cohorts. Together, these differences delineate the specific methodological niche of the present work: advancing the mechanistic resolution of intramural oxLDL dynamics through explicit multi-layer wall transport, macrophage-foam cell signaling, and cytokine-mediated tissue remodeling, and providing longitudinal validation in a controlled preclinical setting that enables direct access to early plaque initiation.

4.1. Clinical relevance

From a translational perspective, the framework has the potential to act as a patient-specific predictor of plaque initiation and vascular remodeling. By modeling with reasonable fidelity the cellular events that underlie wall remodeling, the model provides a mechanistic basis to anticipate spatial patterns of disease progression and, in the future, to support in silico testing of therapeutic strategies. While the current implementation is not yet prepared for such applications, it establishes the foundation for probing how targeted interventions might alter disease trajectories. For instance, if chronic inflammation is hypothesized to contribute to unstable plaques through exaggerated immune activation, the framework could be used to explore the potential effects of reducing macrophage recruitment, slowing vSMC proliferation or migration, or modulating cytokine-mediated feedback.

An additional clinically relevant extension concerns calcification, a complex process involving multiple proposed mechanisms that are not explicitly represented in the current model. Although processes such as sSMC death and impaired efferocytosis may contribute to its development [75], they are unlikely to fully account for this phenomenon. Even so, by representing key cellular and biochemical interactions involved in plaque progression, the present framework may offer a useful starting point for future extensions aimed at incorporating calcification. Such developments, however, will require further mechanistic refinement and dedicated quantitative validation as more specific data become available.

More generally, the framework estimates the tendency of wall remodeling, lumen stenosis, and necrotic core formation in low-TAWSS regions, all of which are key for identifying high-risk segments. Although TAWSS is not the sole driver of atherosclerosis—systemic comorbidities such as diabetes, smoking, or obesity are also major contributors—the established link between TAWSS, endothelial permeability, and oxLDL infiltration provides a mechanistic substrate that remains valid under different comorbid conditions. In this context, the added value of our framework lies in its capacity to move beyond the mere identification of atheroprone zones from static TAWSS maps: it mechanistically reconstructs the evolving plaque microenvironment, enabling predictions not only of lesion location but also of internal composition (e.g., spatial distributions of macrophages, sSMCs, ECM, and lipid-rich necrotic cores) and of emergent feedback between hemodynamics, oxLDL accumulation, and tissue expansion.

4.2. Limitations

Despite its strengths, the present framework is subject to several limitations that should be considered when interpreting the results. Validation was restricted to a nine-month follow-up in four porcine arteries, which limits statistical power and prevents extrapolation to longer-term disease dynamics. Longer longitudinal follow-up under comparable in vivo conditions would help clarify the true time scales of plaque progression and enable tighter parameter calibration. The primary limitation of the present study is the limited number of animals and vessels, a constraint largely imposed by the availability of high-resolution invasive imaging and Doppler-based flow measurements. Although the validation was spatially extensive within each artery, comprising 50 cross-sections per artery ($n = 200$ for SR) and 8 sector-level comparisons per cross-section ($n = 1600$ for ΔWT), these observations should be interpreted as within-artery replication rather than as an increase in cohort size. Accordingly, larger cohorts and external validation datasets will be required to quantify inter-subject variability, test generalizability, and strengthen statistical inference. In addition, the OCT-derived dataset provided only binary information on plaque presence in certain sections, precluding detailed calibration of plaque morphology and composition.

Furthermore, the current mass transport module uses TAWSS as the hemodynamic input to modulate endothelial permeability. While this choice is consistent with the adopted permeability formulation and is widely used in the literature [28–30,51], it does not fully capture the multidirectional and oscillatory nature of coronary shear. Complementary descriptors such as the Oscillatory Shear Index (OSI), Relative Residence Time (RRT), or transverse WSS (transWSS) are known to better characterize disturbed flow [31], and their integration into the present framework should be investigated in future work. Moreover, coronary motion was neglected and vessels were modeled as rigid, fixed geometries. Because LAD and RCA are epicardial arteries subjected to cardiac motion, dynamic deformation may influence instantaneous shear patterns. Although the use of TAWSS mitigates sensitivity to transient geometric variations, incorporating vessel motion or fluid–structure interaction frameworks could further refine local hemodynamic predictions in future studies.

The framework also lacked specific experimental measurements of key cellular parameters in porcine coronary arteries, such as cytokine secretion rates, proliferation rates, or migration speeds of vSMCs under pathological oxLDL exposure. As a result, some rules relied on fitted parameters and therefore remained calibration-dependent rather than independently validated. Similarly, macrophage-related processes—including recruitment dynamics, phagocytosis rates, and maximum

oxLDL uptake capacity—could not be directly constrained, and ECM production could not be validated against quantitative measurements. This limitation is shared by most mechanistic or multiscale models of atherosclerosis, which often rely on experimentally reported ranges or human-derived estimates for macrophage kinetics and ECM turnover [36,41,61]. Finally, the model necessarily simplifies cellular dynamics due to both data scarcity and computational cost. Cytokines were represented only as pro-inflammatory signals rather than as individual pro- and anti-inflammatory species with distinct effects, which limits the fidelity of immune regulation. Taken together, these limitations imply that, although the framework robustly captures macroscopic features of disease progression, the underlying cellular mechanisms remain only partially constrained and should therefore be interpreted with caution.

4.3. Future directions

Looking forward, several improvements could further enhance the framework. On the biological side, incorporating macrophage heterogeneity (e.g., M1 pro-inflammatory and M2 anti-inflammatory phenotypes) would allow the model to address regression and stabilization processes that were outside the scope of the present study but are highly relevant for therapeutic development. Rules for fibrous-cap composition and ECM turnover have already been implemented, but they require dedicated validation against experimental data to increase confidence in predictions of plaque vulnerability. Extending the framework to incorporate calcification would also represent an important step toward capturing more advanced lesion phenotypes. In addition, future extensions could leverage molecular measurements when available. For instance, transcriptomic or proteomic profiles of lesional tissue may provide independent constraints to inform macrophage polarization, vSMC phenotypic switching, and inflammatory signaling intensity, thereby reducing reliance on fitted rules and improving biological specificity.

From a hemodynamic and mechanical perspective, future work could refine the representation of vascular loading and flow disturbance. In particular, integrating complementary hemodynamic descriptors such as OSI, RRT, or transWSS into the mechanobiological coupling equations could provide a more nuanced representation of disturbed coronary flow and help determine whether these indices improve predictive performance beyond TAWSS alone. Likewise, coupling the framework with models that compute wall stresses and strains could improve estimates of structural loading and cap rupture risk, while incorporating coronary motion or fluid–structure interaction may further refine local hemodynamic predictions.

In parallel, future work would benefit from a formal multiscale uncertainty quantification strategy. While the CFD and mass-transport submodels rely on previously validated formulations and calibration was restricted here to selected ABM parameters, a component-wise error decomposition coupled with global sensitivity analysis would help quantify how uncertainties propagate across scales and identify the dominant contributors to prediction error. Although the present study performed calibration and validation at the cross-sectional level to remain consistent with the dimensionality of the available NIRS-IVUS and OCT measurements, future developments could explore full 3D calibration and validation strategies as volumetric compositional datasets become available. Hybrid multiscale frameworks addressing other vascular pathologies have successfully implemented full-artery 3D calibration approaches [37,38], demonstrating the feasibility of such strategies when volumetric ground truth is accessible. Extending the present framework toward volumetric compositional validation would enable direct assessment of longitudinal plaque evolution and further strengthen its multiscale predictive capability. Finally, larger validation datasets combining long-term longitudinal imaging with molecular characterization will be essential to better constrain intermediate cellular processes, reduce reliance on fitted parameters, and support future translation toward patient-specific predictive applications.

5. Conclusions

This validation study indicates that our multiscale hybrid framework—combining 3D hemodynamics to compute TAWSS, 2D mass transport to quantify LDL filtration and oxLDL accumulation within the arterial wall, and an ABM to simulate the main cellular events underlying atherosclerosis—can translate baseline hemodynamic patterns into realistic predictions of stenosis progression and wall thickening.

The simulations stratified arterial sectors according to their hemodynamic exposure: low-TAWSS regions preferentially developed eccentric wall growth, lumen narrowing, and lipid accumulation, whereas high-TAWSS regions remained comparatively stable. The framework also proved valuable in recapitulating the localization of lipid-rich segments and in predicting the emergence of necrotic cores in low-TAWSS regions.

Overall, the results highlight the potential of such multiscale hybrid models as tools for preclinical research. With further validation and targeted extensions—including improved calibration of cellular parameters, validation of ECM and fibrous-cap dynamics, and incorporation of advanced lesion features such as calcification—the framework could evolve into a predictive platform for patient-specific risk assessment and for virtual testing of therapeutic strategies.

CRediT authorship contribution statement

Ricardo Caballero: Writing – review & editing, Writing – original draft, Visualization, Validation, Software, Methodology, Investigation, Data curation, Conceptualization. **Miguel Ángel Martínez:** Conceptualization, Supervision. **Jolanda J. Wentzel:** Resources, Data curation. **Ali C. Akyildiz:** Resources, Data curation, Supervision, Writing – review & editing. **Estefanía Peña:** Conceptualization, Methodology, Supervision, Funding acquisition, Writing – review & editing.

Ethical statement

This research presents an accurate account of the work performed, all data presented are accurate and methodologies are detailed enough to permit others to replicate the work.

This manuscript represents entirely original works and if work and/or words of others have been used, they have been appropriately cited or quoted and permission has been obtained where necessary.

This material has not been published in whole or in part elsewhere. The manuscript is not currently being considered for publication in another journal. That generative AI and AI-assisted technologies have not been utilized in the writing process or if used, their use has been disclosed in the manuscript and a statement will appear in the published work.

That generative AI and AI-assisted technologies have not been used to create or alter images unless specifically used as part of the research design where such use must be described in a reproducible manner in the methods section.

All authors have been personally and actively involved in substantive work leading to the manuscript and will hold themselves jointly and individually responsible for its content.

Declaration of competing interests

The authors declare the following financial interests/personal relationships that may be considered potential competing interests:

Ricardo Caballero reports that financial support was provided by the Spanish Ministry of Science and Technology through research project PDI2022-140219OB-I00, as well as by the regional Government of Aragón for the funding of the research project PRE2020-095671. If there are other authors, they declare that they have no known competing

financial interests or personal relationships that could have appeared to influence the work reported in this paper.

References

[1] G.A. Roth, G.A. Mensah, C.O. Johnson, G. Addolorato, E. Ammirati, L.M. Baddour, N.C. Barengo, A.Z. Beaton, E.J. Benjamin, C.P. Benziger, et al., Global burden of cardiovascular diseases and risk factors, 1990–2019: update from the GBD 2019 study, J. Am. Coll. Cardiol. 76 (2020) 2982–3021.

[2] E. Wilkins, L. Wilson, K. Wickramasinghe, P. Bhatnagar, J. Leal, R. Luengo-Fernandez, R. Burns, M. Rayner, N. Townsend, European cardiovascular disease statistics 2017, European Heart Network, Brussels, 2017.

[3] World Health Organization, cardiovascular diseases (CVDs), 2021, https://www.who.int/news-room/fact-sheets/detail/cardiovascular-diseases-(cvds), (Accessed: 26 July 2022).

[4] C. Pederiva, M.E. Capra, C. Viggiano, V. Rovelli, G. Banderali, G. Biasucci, Early prevention of atherosclerosis: detection and management of hypercholesterolaemia in children and adolescents, Life 11 (2021) 345.

[5] A.V. Poznyak, N.K. Sadykhov, A.G. Kartuesov, E.E. Borisov, A.A. Melnichenko, A.V. Grechko, A.N. Orekhov, Hypertension as a risk factor for atherosclerosis: cardiovascular risk assessment, Front. Cardiovasc. Med. 9 (2022) 959285.

[6] S.S. Martin, M.J. Blaha, R. Blankstein, A. Agatston, J.J. Rivera, S.S. Virani, P. Ouyang, S.R. Jones, R.S. Blumenthal, M.J. Budoff, et al., Dyslipidemia, coronary artery calcium, and incident atherosclerotic cardiovascular disease: implications for statin therapy from the multi-ethnic study of atherosclerosis, Circulation 129 (2014) 77–86.

[7] E. Hasheminasabgorji, J.C. Jha, Dyslipidemia, diabetes and atherosclerosis: role of inflammation and ROS-redox-sensitive factors, Biomedicines 9 (2021) 1602.

[8] F. Ito, Y. Sono, T. Ito, Measurement and clinical significance of lipid peroxidation as a biomarker of oxidative stress: oxidative stress in diabetes, atherosclerosis, and chronic inflammation, Antioxidants 8 (2019) 72.

[9] P.-Y. Chen, L. Qin, N. Baeyens, G. Li, T. Afolabi, M. Budatha, G. Tellides, M.A. Schwartz, M. Simons, et al., Endothelial-to-mesenchymal transition drives atherosclerosis progression, J. Clin. Invest. 125 (2015) 4514–4528.

[10] Y. Yoshimatsu, T. Watabe, Emerging roles of inflammation-mediated endothelial-mesenchymal transition in health and disease, Inflamm. Regen. 42 (2022) 9.

[11] R.J. Esper, R.A. Nordaby, J.O. Vilariño, A. Paragano, J.L. Cacharrón, R.A. Machado, Endothelial dysfunction: a comprehensive appraisal, Cardiovascular Diabetology 5 (2006) 1–18.

[12] A.M. Malek, S.L. Alper, S. Izumo, Hemodynamic shear stress and its role in atherosclerosis, Jama 282 (1999) 2035–2042.

[13] S. Jebari-Benslaiman, U. Galicia-García, A. Larrea-Sebal, J.R. Olaetxea, I. Alloza, K. Vandenbroeck, A. Benito-Vicente, C. Martín, Pathophysiology of atherosclerosis, Int. J. Mol. Sci. 23 (2022) 3346.

[14] S. Glagov, E. Weisenberg, C.K. Zarins, R. Stankunavicius, G.J. Kolettis, Compensatory enlargement of human atherosclerotic coronary arteries, N. Engl. J. Med. 316 (1987) 1371–1375.

[15] E.M.J. Hartman, G. De Nisco, F.J.H. Gijsen, S.-A. Korteland, A.F.W. van der Steen, J. Daemen, J.J. Wentzel, The definition of low wall shear stress and its effect on plaque progression estimation in human coronary arteries, Sci. Rep. 11 (2021) 22086.

[16] C.G. Caro, J.M. Fitz-Gerald, R.C. Schroter, Atheroma and arterial wall shear-observation, correlation and proposal of a shear dependent mass transfer mechanism for atherogenesis, Proceedings of the Royal Society of London. Series B. Biological Sciences 177 (1971) 109–133.

[17] I. Tabas, K.J. Williams, J. Borén, Subendothelial lipoprotein retention as the initiating process in atherosclerosis, Circulation 116 (2007) 1832–1844.

[18] K.-W. Kim, S. Ivanov, J.W. Williams, Monocyte recruitment, specification, and function in atherosclerosis, Cells 10 (2020) 15.

[19] T.J. Barrett, Macrophages in atherosclerosis regression, Arterioscler. Thromb. Vasc. Biol. 40 (2020) 20–33.

[20] P. Libby, J.E. Buring, L. Badimon, G.K. Hansson, J. Deanfield, M.S. Bittencourt, L. Tokgözoğlu, E.F. Lewis, Atherosclerosis, Nat. Rev. Dis. Primers 5 (2019) 56.

[21] A.J. Lusis, Atherosclerosis, Nature 407 (2000) 233–241.

[22] D. Gomez, G.K. Owens, Smooth muscle cell phenotypic switching in atherosclerosis, Cardiovasc. Res. 95 (2012) 156–164.

[23] R.A. Sukhovershin, N.E.T. Furman, E. Tasciotti, B.H. Trachtenberg, Local inhibition of macrophage and smooth muscle cell proliferation to suppress plaque progression, Methodist DeBakey Cardiovasc. J. 12 (2016) 141–145.

[24] R. Nakano-Kurimoto, K. Ikeda, M. Uraoka, E. al., Replicative senescence of vascular smooth muscle cells enhances the calcification through initiating the osteoblastic transition, Am. J. Physiol. Heart Circ. Physiol. 297 (2009) H1673–H1684.

[25] M.R. Bennett, R. Virmani, Vascular smooth muscle cells in atherosclerosis, Circ. Res. 118 (2016) 692–702.

[26] B. Keller, F. Clubb Jr, G. Dubini, A review of atherosclerosis and mathematical transport models, in: International Conference on Advancements of Medicine and Health Care Through Technology: 29th August–2nd September 2011, Cluj-Napoca, Romania, Springer, 2011, pp. 338–343.

[27] A. Corti, M. Colombo, G. De Nisco, J.F. Rodriguez Matas, F. Migliavacca, C. Chiastra, Chapter 6 - computational investigation of the role of low-density lipoprotein and oxygen transport in atherosclerotic arteries, in: S. Becker, A.V. Kuznetsov, F. de Monte, G. Pontrelli, D. Zhao (Eds.), Modeling of Mass Transport Processes in Biological Media, Academic Press, 2022, pp. 139–213.

[28] P. Hernández-López, M. Cilla, M. Martínez, E. Peña, Effects of the haemodynamic stimulus on the location of carotid plaques based on a patient-specific mechanobiological plaque atheroma formation model, Front. Bioeng. Biotechnol. 9 (2021) 690685.

[29] U. Olgac, V. Kurtcuoglu, D. Poulikakos, Computational modeling of coupled blood-wall mass transport of ldl: effects of local wall shear stress, Am. J. Physiol. Heart Circ. Physiol. 294 (2008) H909–H919.

[30] M. Cilla, J. Martinez, E. Pena, M.Á. Martínez, Machine learning techniques as a helpful tool toward determination of plaque vulnerability, IEEE Trans. Biomed. Eng. 59 (2012) 1155–1161.

[31] G. De Nisco, E.M.J. Hartman, E. Torta, J. Daemen, C. Chiastra, D. Gallo, U. Morbiducci, J.J. Wentzel, Predicting lipid-rich plaque progression in coronary arteries using multimodal imaging and wall shear stress signatures, Arterioscler. Thromb. Vasc. Biol. 44 (2024) 976–986.

[32] P. Hernandez-Lopez, N. Laita, M. Cilla, M.Á. Martínez, E. Pena, Impact of hypertension and arterial wall expansion on transport properties and atherosclerosis progression, J. Biomech. 174 (2024) 112212.

[33] P. Hernández-López, M. Cilla, M.A. Martinez, E. Pena, M. Malve, Impact of geometric and hemodynamic changes on a mechanobiological model of atherosclerosis, Comput. Methods Programs Biomed. 254 (2024) 108296.

[34] P. Hernández-López, M.A. Martínez, E. Peña, M. Cilla, Understanding the parameter influence on lesion growth for a mechanobiology model of atherosclerosis, Mathematics 11 (2023) 829.

[35] T.N.A.M. Vuong, M. Bartolf-Kopp, K. Andelovic, T. Jungst, N. Farbehi, S.G. Wise, C. Hayward, M.C. Stevens, J. Rnjak-Kovacina, Integrating computational and biological hemodynamic approaches to improve modeling of atherosclerotic arteries, Adv. Sci. 11 (2024) 2307627.

[36] A. Corti, M. Colombo, F. Migliavacca, J.F. Rodriguez Matas, S. Casarin, C. Chiastra, Multiscale computational modeling of vascular adaptation: a systems Biology approach using agent-based models, Front. Bioeng. Biotechnol. 9 (2021) 744560.

[37] A. Corti, M. Colombo, J.M. Rozowsky, S. Casarin, Y. He, D. Carbonaro, F. Migliavacca, J.F. Rodriguez Matas, S.A. Berceli, C. Chiastra, A predictive multiscale model of in-stent restenosis in femoral arteries: linking haemodynamics and gene expression with an agent-based model of cellular dynamics, J. R. Soc. Interface 19 (2022) 20210871.

[38] A. Corti, F. Migliavacca, S.A. Berceli, C. Chiastra, Predicting 1-year in-stent restenosis in superficial femoral arteries through multiscale computational modelling, J. R. Soc. Interface 20 (2023) 20220876.

[39] N. Hampwaye, J. Wang, A. Revell, E. Manchester, T. Aldersley, L. Zuhlke, B. Keavney, M. Ngoepe, Growth in a two-dimensional model of coarctation of the aorta: a cfd-informed agent based model, J. Biomech. 182 (2025) 112514.

[40] A. Corti, C. Chiastra, M. Colombo, M. Garbey, F. Migliavacca, S. Casarin, A fully coupled computational fluid dynamics–agent-based model of atherosclerotic plaque development: multiscale modeling framework and parameter sensitivity analysis, Comput. Biol. Med. 118 (2020) 103623.

[41] R. Caballero, M.A. Martinez, E. Peña, Fully coupled hybrid in-silico modeling of atherosclerosis: a multi-scale framework integrating CFD, transport phenomena and agent-based modeling, Front. Bioeng. Biotechnol. 13 (2025) 1549104.

[42] A. Corti, G. De Nisco, J.J. Wentzel, F. Migliavacca, U. Morbiducci, C. Chiastra, Personalized multiscale modeling of coronary plaque progression: the interaction between low-density-lipoprotein transport and cellular dynamics, Comput. Methods Appl. Mech. Eng. 448 (2026) 118427.

[43] G. De Nisco, C. Chiastra, E.M.J. Hartman, A. Hoogendoorn, J. Daemen, K. Calò, D. Gallo, U. Morbiducci, J.J. Wentzel, Comparison of swine and human computational hemodynamics models for the study of coronary atherosclerosis, Front. Bioeng. Biotechnol. 9 (2021) 731924.

[44] A. Hoogendoorn, S. den Hoedt, E.M.J. Hartman, I. Krabbendam-Peters, M. te Lintel Hekkert, L. van der Zee, K. van Gaalen, K.T. Witberg, K. Dorst, J.M.R. Ligthart, et al., Variation in coronary atherosclerosis severity related to a distinct ldl (low-density lipoprotein) profile: findings from a familial hypercholesterolemia pig model, Arterioscler. Thromb. Vasc. Biol. 39 (2019) 2338–2352.

[45] G. De Nisco, A.M. Kok, C. Chiastra, D. Gallo, A. Hoogendoorn, F. Migliavacca, J.J. Wentzel, U. Morbiducci, The atheroprotective nature of helical flow in coronary arteries, Ann. Biomed. Eng. 47 (2019) 425–438.

[46] P. Libby, Current concepts of the pathogenesis of the acute coronary syndromes, Circulation 104 (2001) 365–372.

[47] C.C. Michel, F.E. Curry, Microvascular permeability, Physiol. Rev. 79 (1999) 703–761.

[48] M.J. Levesque, D. Liepsch, S. Moravec, R.M. Nerem, Correlation of endothelial cell shape and wall shear stress in a stenosed dog aorta, Arteriosclerosis 6 (1986) 220–229.

[49] O. Kedem, A. Katchalsky, Thermodynamic analysis of the permeability of biological membranes to non-electrolytes, Biochim. Biophys. Acta 27 (1958) 229–246.

[50] G. Meyer, R.G. Merval, A. Tedgui, Effects of pressure-induced stretch and convection on low-density lipoprotein and albumin uptake in the rabbit aortic wall, Circ. Res. 79 (1996) 532–540.

[51] L. Ai, K. Vafai, A coupling model for macromolecule transport in a stenosed arterial wall, Int. J. Heat Mass Transf. 49 (2006) 1568–1591.

[52] A. Tedgui, M.J. Lever, Filtration through damaged and undamaged rabbit thoracic aorta, Am. J. Physiol. Heart Circ. Physiol. 247 (1984) H784–H791.

[53] W.R. Milnor, Hemodynamics, Williams & Wilkins, Baltimore, MD, 1989.

[54] M. Dabagh, P. Jalali, J.M. Tarbell, The transport of ldl across the deformable arterial wall: the effect of endothelial cell turnover and intimal deformation under hypertension, Am. J. Physiol. Heart Circ. Physiol. 297 (2009) H983–H996.

[55] S. Weinbaum, G. Tzeghai, P. Ganatos, R. Pfeffer, S. Chien, Effect of cell turnover and leaky junctions on arterial macromolecular transport, Am. J. Physiol. Heart Circ. Physiol. 248 (1985) H945–H960.
[56] J.M. Tarbell, Mass transport in arteries and the localization of atherosclerosis, Annu. Rev. Biomed. Eng. 5 (2003) 79–118.
[57] Ž. Reiner, A.L. Catapano, G. De Backer, I. Graham, M.-R. Taskinen, O. Wiklund, S. Agewall, E. Alegria, M.J. Chapman, P. Durrington, et al., ESC/EAS guidelines for the management of dyslipidaemias: the task force for the management of dyslipidaemias of the european society of cardiology (esc) and the european atherosclerosis society (eas), Eur. Heart J. 32 (2011) 1769–1818.
[58] U. Wilensky, NetLogo, Center for Connected Learning and Computer-Based Modeling, Northwestern University, 1999. Version 6.1.
[59] G.M. Cooper ed, The Cell: A Molecular Approach, second ed, Sinauer Associates Inc., Sunderland, MA, 2000.
[60] A.L. Olivares, M.A. González Ballester, J. Noailly, Virtual exploration of early stage atherosclerosis, Bioinformatics 32 (2016) 3798–3806.
[61] R. Bhui, H.N. Hayenga, An agent-based model of leukocyte transendothelial migration during atherogenesis, PLOS Comput. Biol. 13 (2017) e1005523.
[62] P.E. Hart, N.J. Nilsson, B. Raphael, A formal basis for the heuristic determination of minimum cost paths, IEEE Trans. Syst. Sci. Cybern. 4 (1968) 100–107.
[63] M. Garbey, M. Rahman, S. Berceli, A multiscale computational framework to understand vascular adaptation, J. Comput. Sci. 8 (2015) 32–47.
[64] B.C. Isenberg, P.A. DiMilla, M. Walker, S. Kim, J. Wong y, Vascular smooth muscle cell durotaxis depends on substrate stiffness gradient strength, Biophys. J. 97 (2009) 1313–1322.
[65] M.R. Zanotelli, J.P. Miller, W. Wang, I. Ortiz, E. Tahon, F. Bordeleau, C.A. Reinhart-King, Tension directs cancer cell migration over fiber alignment through energy minimization, Biomaterials 311 (2024) 122682.
[66] C.J. Boyle, A.B. Lennon, P.J. Prendergast, In silico prediction of the mechanobiological response of arterial tissue: application to angioplasty and stenting, J. Biomech. Eng. 133 (2011) 081001.
[67] J. Escuer, M.A. Martínez, S. McGinty, E. Peña, Mathematical modelling of the restenosis process after stent implantation, J. R. Soc. Interface 16 (2019) 20190313.
[68] H. Zahedmanesh, H. Van Oosterwyck, C. Lally, A multi-scale mechanobiological model of in-stent restenosis: deciphering the role of matrix metalloproteinase and extracellular matrix changes, Computer Methods in Biomechanics and Biomedical Engineering 17 (2014) 813–828.
[69] F.H. Khan, F. Khan, The Elements of Immunology, Pearson Education India, 2009.
[70] D. Steinberg, J.C. Khoo, C.K. Glass, W. Palinski, F. Almazan, A new approach to determining the rates of recruitment of circulating leukocytes into tissues: application to the measurement of leukocyte recruitment into atherosclerotic lesions, Proc. Natl. Acad. Sci. 94 (1997) 4040–4044.
[71] M.A.K. Bulelzai, J. Dubbeldam la, Long time evolution of atherosclerotic plaques, J. Theor. Biol. 297 (2012) 1–10.
[72] W. Zhao, C.A. Oskeritzian, A.L. Pozez, L.B. Schwartz, Cytokine production by skin-derived mast cells: endogenous proteases are responsible for degradation of cytokines, J. Immunol. 175 (2005) 2635–2642.
[73] E. Kuhl, R. Maas, G. Himpel, A. Menzel, Computational modeling of arterial wall growth: attempts towards patient-specific simulations based on computer tomography, Biomech. Model. Mechanobiol. 6 (2007) 321–331.
[74] J.D. Humphrey, M.A. Schwartz, Vascular mechanobiology: homeostasis, adaptation, and disease, Annu. Rev. Biomed. Eng. 23 (2021) 1–27.
[75] A.L. Durham, M. Speer y, M. Scatena, C.M. Giachelli, C.M. Shanahan, Role of smooth muscle cells in vascular calcification: implications in atherosclerosis and arterial stiffness, Cardiovasc. Res. 114 (2018) 590–600.